Available on CMS information server

CMS NOTE 2006/115

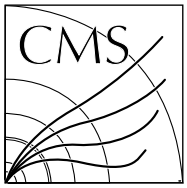

The Compact Muon Solenoid Experiment

CMS Note

Mailing address: CMS CERN, CH-1211 GENEVA 23, Switzerland

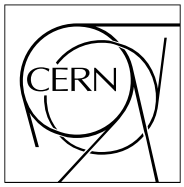

30th June 2006

Discovery potential for the SM Higgs boson in the $\mathbf{H \longrightarrow ZZ^{(*)} \longrightarrow e^+e^-e^+e^-}$ decay channel

S. Baffioni [a)], C. Charlot [a)], F. Ferri [a) b)], N. Godinovic [c)], P. Meridiani [d)], I. Puljak [c)], R. Salerno [a) b)], Y. Sirois [a)]

a) Laboratoire Leprince-Ringuet, Ecole Polytechnique and IN2P3-CNRS, Palaiseau, France

b) Università di Milano Bicocca and INFN Milano, Milano, Italy

c) Technical University of Split, FESB, Croatia

d) Università di Roma I and INFN, Rome, Italy

Abstract

A prospective analysis is presented for the discovery and for the mass and cross-section measurements of the Standard Model Higgs boson in the CMS experiment at the LHC collider. The analysis focuses on the $\mathrm{pp} \rightarrow \mathrm{H} + \mathrm{X} \rightarrow \mathrm{ZZ}^{(*)} + \mathrm{X} \rightarrow \mathrm{e^+e^-e^+e^-} + \mathrm{X}$ channel for Higgs boson masses in the range $120 \lesssim m_{\mathrm{H}} \lesssim 300$ GeV$/c^2$. It relies on a full simulation of the detector response and usage of new detailed electron reconstruction tools. Emphasis is put on realistic strategies for the evaluation of experimental systematics and control of physics background processes. For an integrated LHC luminosity of 30 fb^{-1}, a Standard Model Higgs boson would be observed in the $\mathrm{e^+e^-e^+e^-}$ channel with a significance above 3 standard deviations for masses m_{H} in the range from about 130 to 160 GeV$/c^2$ and above 180 GeV$/c^2$. A discovery with a significance above 5 standard deviations is possible for this integrated luminosity around $m_{\mathrm{H}} \simeq 150$ GeV$/c^2$ and in the range from about 190 to 300 GeV$/c^2$. The mass (cross-section) of the Higgs boson can be determined with a precision better than 0.5% (30%).

1 Introduction

The Standard Model (SM) of electroweak interactions contains a unique physical Higgs boson of mass $m_{\rm H}$. One of the most promising channel for the search of this postulated boson at the future LHC pp collider is the single production mode followed by a decay in a $\rm ZZ^{(*)}$ pair. This inclusive process $pp \rightarrow \rm H + \mathit{X} \rightarrow ZZ^{(*)} + X$ is on the critical path of a discovery at the LHC, over an extended range of possible $m_{\rm H}$ values.

The value of $m_{\rm H}$ is a free parameter of the SM which must be constrained by experiments. The range of $m_{\rm H}$ values at or below the Fermi scale, a scale characteristic of the unification of electromagnetic and weak interactions, is found to be of particular interest. The Higgs boson contributes in radiative corrections to electroweak observables. A consistency fit of electroweak precision data carried out in the SM framework yields an indirect constraint of $m_{\rm H} < 237$ GeV$/c^2$ (95% CL)[1]. Direct searches for the SM Higgs particle at the LEP $\rm e^+e^-$ collider have lead to a strict lower mass bound of 114.4 GeV$/c^2$ (95% CL) [1]. Ongoing direct searches at the Tevatron II $p\bar{p}$ collider by the D0 and CDF experiments could allow to further constrain $m_{\rm H}$, to values above $\simeq 120$ GeV$/c^2$ [2], before the commissioning of the LHC. In this note, the discovery potential of the CMS experiment for the SM Higgs boson is discussed in the mass range of $120 \lesssim m_{\rm H} \lesssim 300$ GeV$/c^2$, focusing on the decay chain $\rm H \rightarrow ZZ^{(*)} \rightarrow e^+e^-e^+e^-$.

The analysis relies on a detailed simulation of the detector response in the experimental conditions of the first years of low luminosity LHC running. The CMS detector has been described elsewhere [3]. The simulation of the signal and background processes used for this prospective is described in Section 2. The detailed High Level Trigger and reconstruction algorithms used at each step of this analysis have been presented in Ref. [4]. The electron reconstruction plays a special role in the event signature and is discussed here in more detail in Section 3. Basic, and in part compulsory, triggering and pre-selection steps for data reduction are described in Section 4. The optimization of a simple sequential set of requirements for primary electrons and for the event kinematics is presented in Section 5. The selection is optimized to preserve a best signal detection efficiency and highest significance for a discovery, while allowing for a control of experimental systematics and of systematics on physics background rates. Realistic strategies for the taming and measurements of systematics are described in Section 6. Results on the expected discovery reach of the SM Higgs boson in CMS in the $\rm H \rightarrow ZZ^{(*)} \rightarrow e^+e^-e^+e^-$ channel and for the measurement of its mass, width and cross-section are finally presented in Section 7.

2 Signal and Background Processes

2.1 General Description

The inclusive single Higgs boson production benefits from a high production cross-section at the LHC of about 40×10^3 fb (NLO) at $m_{\rm H} = 130$ GeV$/c^2$, decreasing monotically to about 10×10^3 fb around $m_{\rm H} = 300$ GeV$/c^2$. The production cross-section is dominated ($\gtrsim 80\%$) in this mass range by gluon-gluon fusion processes via triangular loops involving heavy quark (mostly the top quark) flavours. The branching ratio in the SM for the $\rm H \rightarrow Z^{(*)}Z^{(*)}$ decay is sizeable ($\gtrsim 1\%$) for any $m_{\rm H}$ value above about 115 GeV$/c^2$. It rises to a peak value above 8% around $m_{\rm H} \simeq 150$ GeV$/c^2$ and is suppressed around $m_{\rm H} \simeq 2 \times m_{\rm W}$. For $m_{\rm H} \geq 2 \times m_{\rm Z}$, it reaches a plateau of 20 to 30%. The $\rm ZZ^{(*)}$ contribution, i.e. with at least one Z boson on its mass shell, is greater than 50% for $m_{\rm H} \gtrsim 115$ GeV$/c^2$, and greater than 85% for $m_{\rm H} \gtrsim 150$ GeV$/c^2$. Thus, the $\rm H \rightarrow ZZ^{(*)} \rightarrow e^+e^-e^+e^-$ (in short $\rm H \rightarrow 4e$) channel offers a possibly significant, very clean and simple multi-lepton final state signature.

A main background source of four electrons final states arises from non-resonant SM continuum production of $\rm Z^{(*)}/\gamma^*Z^{(*)}/\gamma^*$ and the production of real ZZ pairs which proceeds dominantly via quark-antiquark annihilation. This constitutes an irreducible background which will be hereafter referred to as the "$\rm ZZ^{(*)}$" background. Other $\rm 4e$ background sources come from pair production of heavy quark flavours such as the $\rm t\bar{t}$ production and the $\rm Z^{(*)}/\gamma^*b\bar{b}$ associated production mediated by QCD, and which proceed dominantly via gluon-gluon fusion. These will be hereafter referred to as the "$\rm t\bar{t}$" and "$\rm Zb\bar{b}$" background processes.

Additional contributions could in principle come from misidentified $\rm 4e$ events in which "fake primary electrons" are reconstructed due to early photon conversions in the CMS detector, or are produced in QCD jets from leptonic and semi-leptonic meson and baryon decays or from $\pi^0\pi^\pm$ hadron overlaps. A potentially dangerous misidentified background comes from $\rm Z + jet(s)$ Drell-Yan production at NLO in which the Z boson recoils against the jet(s). This kind of misidentified backgrounds have been studied more extensively in Ref. [5]. The suppression of the $\rm Z + jet(s)$ background via electron identification and kinematics is further discussed here in Section 5.1.

2.2 Simulation

All signal and background processes are simulated for pp collisions at the LHC at a centre-of-mass energy $\sqrt{s_{\rm pp}} = 14$ TeV with pile-up conditions from multiple collisions as expected in the low luminosity collider machine configuration of 2×10^{33} cm^{-2}s^{-1} (of $\mathcal{O}(10)$ fb^{-1}/year). The non-perturbative parton density functions (PDFs) in the proton are taken from the so-called CTEQ6 distributions [6] which were obtained in 2002 from a global QCD analysis combining all existing relevant deep inelastic and jet cross-section measurement results. For the analysis, all event sample cross-sections are normalized to next-to-leading-order (NLO) calculations. Signal, ZZ$^{(*)}$ and Zb$\bar{\rm b}$ background event generators are interfaced with PHOTOS [7] for the simulation of QED final state radiations.

The H $\rightarrow$ 4e signal samples are generated with PYTHIA [8] (version 6.223) using the CMS interface CMKIN [9] (version 3.1.0). The Higgs boson is produced via either gluon fusion or weak boson fusion processes, and forced to decay into a Z boson pair. The Z bosons are subsequently forced to undergo a decay in an electron-positron pair. A set of 12 different samples is used in this analysis, with Higgs boson masses ranging from 115 to 300 GeV/c^2. These are listed in Table 1. The generated signal samples are normalized to the value of the total cross-section at NLO [10], including all Higgs boson production processes and multiplied by the branching ratios BR(H $\rightarrow$ ZZ$^{(*)}$) [11] and BR(Z $\rightarrow$ e$^+$e$^-$) [12]. An additional enhancement of the signal is considered, which is due to the constructive final state interference between like-sign electrons originating from different Z$^{(*)}$ bosons [13]. This enhancement has been re-evaluated with CompHEP [14] and amounts to a factor 1.13 ± 0.01 at $m_{\rm H} = 115$ GeV/c^2, slowly decreasing to a negligible value when approaching $m_{\rm H} \approx 2m_{\rm Z}$ [15].

$m_{\rm H}$ (GeV/c^2)	σ_{NLO} (pb)	$\sigma_{NLO} \times BR \times \epsilon_{\rm pres}$ (fb)	$N_{\rm simulated}$
115	47.73	0.27	10000
120	44.30	0.48	10000
130	38.44	1.11	10000
140	33.69	1.78	10000
150	29.81	1.94	10000
160	26.56	0.92	10000
170	23.89	0.43	10000
180	21.59	0.98	10000
190	19.67	3.58	10000
200	17.96	3.94	10000
250	12.37	3.07	10000
300	9.58	2.60	10000
ZZ$^{(*)}$	29.0	20.2	150 000
Zb$\bar{\rm b}$	276.3	120.4	87 000
t$\bar{\rm t}$	840	194.0	500 000

Table 1: Cross-sections at NLO (pb), cross-sections multiplied by branching ratios and by generator pre-selection efficiency (fb), and number of events in data samples after generator pre-selection.

The ZZ$^{(*)}$ background is generated with PYTHIA (version 6.227) using the interface CMKIN (version 4.4.0). This includes only the t-channel contribution with $q\bar{q}$ in the initial state. The missing s-channel might contribute up to 10% for low Higgs boson masses and can be neglected for higher masses [16]. The differential cross-section is re-weighted using $m_{\rm 4e}$ dependent NLO K-factors obtained with MCFM [17], with an average K-factor of $< K_{NLO} >= 1.35$. Both Z bosons are constrained to have a mass within $5 - 150$ GeV/c^2 and are forced to decay into charged lepton pairs, with the τ leptons forced subsequently into e and μ decay channels. The missing gg contribution is estimated to be of the order of 20% at LO [13], with $\pm 8\%$ uncertainties and with unknown NLO K-factors. Recent calculations with TopREX [18] of the production via gluon fusion of two real Z confirm the above estimation. The gg contribution has been shown to remain stable after kinematic cuts in an analysis of the H $\rightarrow$ ZZ$^{(*)}$ $\rightarrow$ 2e2μ channel [19]. In the following, it is treated as a simple addition to the PYTHIA cross-section.

The t$\bar{\rm t}$ background sample is generated with PYTHIA (version 6.227) using the interface CMKIN (version 4.4.0), with W bosons forced to leptonic decays, τ leptons forced to leptonic channels, and with b quarks left to decay freely. Both gluon fusion and quark annihilation initial states are simulated and the cross-section is normalized to the NLO value of $(840 \pm 5\%({\rm scale}) \pm 3\%({\rm PDF}))$ pb [20].

The Zb$\bar{\rm b}$ background is generated using all lowest order gg $\rightarrow$ e$^+$e$^-$b$\bar{\rm b}$ and q$\bar{\rm q}$ $\rightarrow$ e$^+$e$^-$b$\bar{\rm b}$ diagrams (excluding diagrams involving the SM Higgs boson) calculated with CompHEP (version 4.2) and interfaced with PYTHIA (version 6.227) for parton showering and hadronization. All possible combinations of quarks are considered in the

initial state. The total LO cross-section for $m_{e^+e^-} > 5$ GeV$/c^2$ is 115 pb of which about 89% originate from gg processes, 7.7% involve u-like quarks and 3.2% involve d-like quarks in the initial state. The hadronization and decay of the b quarks are left free. A NLO K-factor of 2.4 ± 0.3 is applied [19].

Signal and background events are pre-selected at generator level for further analysis if they satisfy the following acceptance requirements: $\geq 2e^+$ and $\geq 2e^-$ with a transverse momentum $p_T^e > 5$ GeV$/c$ in $|\eta| < 2.7$. In addition for the $Zb\bar{b}$ background at least two e^+e^- pairs with invariant masses between $5 - 400$ GeV$/c^2$ are required. The cross-sections at NLO and after generator pre-selection, as well as the number of events in the data samples available for analysis after generator pre-selection, are given in Table 1.

The detailed simulation of the detector is performed using the CMS simulation OSCAR [21] (version 3.6.5) based on GEANT4 [22]. The reconstruction of physics objects is performed in ORCA [23] (version 8.7.3 which includes the new electron reconstruction [24] of version 8.13.1).

3 Electron Reconstruction

For Higgs bosons with a mass in the range $m_H \lesssim 300$ GeV$/c^2$, the $ZZ^{(*)} \rightarrow e^+e^-e^+e^-$ final state always involves at least one low p_T^e electron, i.e. an electron with p_T^e well below $m_Z/2 \simeq 45$ GeV$/c^2$. In the m_H range below the Z pair production threshold, where the Z and Z* bosons themselves receive in general only a small transverse momentum, the mean p_T^e of the softest electron falls in a range where a full combination of tracking and calorimetry information becomes important. This softest electron, which couples to the off-shell Z*, typically has $p_T^e \lesssim 10$ GeV$/c$ for masses $m_H < 140$ GeV$/c^2$, as can be inferred from Fig. 1.

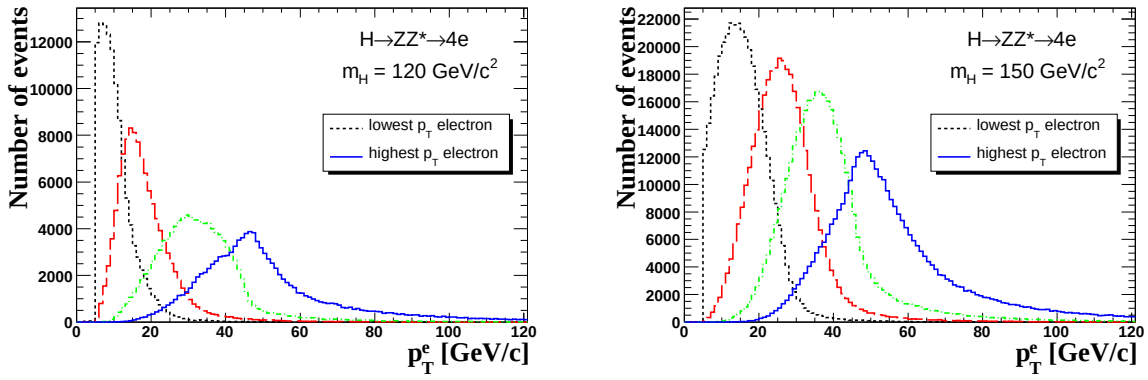

(a) (b)

Figure 1: Generated transverse momentum of final state electrons with $p_T^e > 5$ GeV$/c$ from single Higgs boson production at the LHC in the decay channel $H \rightarrow ZZ^{(*)} \rightarrow e^+e^-e^+e^-$, in two cases: a) for a Higgs mass of 120 GeV$/c^2$, b) for a Higgs mass of 150 GeV$/c^2$.

Hence, an excellent electron reconstruction is essential down to very low p_T^e values, well below the range for which the reconstruction will be best controlled in CMS via measurements with SM single Z and single W production. The control of systematic uncertainties from experimental data is a major issue for such electrons and this will be discussed in detail in Section 6.2. This analysis makes use of the elaborate reconstruction procedures which have been introduced very recently in CMS and have been described in detail in Ref. [24].

The electron identification and momentum measurements are hampered by the amount of tracker material which is distributed in front of the electromagnetic calorimeter (ECAL) [25], and by the presence of a strong magnetic field aligned with the collider beam z axis. Electrons traversing the silicon layers of the tracker radiate bremsstrahlung photons and the energy reaches the ECAL with a significant spread in the azimuthal direction ϕ. The bremsstrahlung emission introduces, in general, non-Gaussian contributions to the event-by-event fluctuations of the calorimetry and tracking measurements. Additional electron tracks from conversion of secondary photons, actually the first stages of an "electromagnetic showering", contribute to the energy lost in front of the ECAL. The procedures introduced in Ref. [24] provide new useful observables that allow to better deal with these detector effects, combining information from the pixel detector [26], the silicon strip tracker [27] and the ECAL.

With respect to the previously available electron reconstruction tools developed in the context of applications for the CMS High Level Trigger (HLT) [28][29], the new electron reconstruction uses a lower threshold (1 GeV) to initiate cluster building and an extended road in ϕ for a better collection of bremsstrahlung. The ECAL supercluster is used to drive the seeding of the tracks in the tracker detector, with hits positions in the pixel layers predicted

by the propagation of the energy weighted mean position of the supercluster backward through the magnetic field under both charge hypotheses. The requirements for the search of the first and second pixel hits have been loosened with respect to those of the HLT. Starting from the seed, a trajectory is created. The track building relies on the Bethe-Heitler modelling of the electron energy losses and a Gaussian Sum Filter (GSF) is used for the forward and backward fits. The track momentum is taken from the most probable value of the mixture of the Gaussian distributions available for each hit position. The relative difference between the momenta measured at both track ends, $f_{\rm brem} = (p_{\rm in} - p_{\rm out})/p_{\rm in}$ is a measure of the fraction of the electron initial energy emitted via bremsstrahlung in the tracker.

The quantity $f_{\rm brem}$ together with other observables sensitive to the amount of bremsstrahlung radiated along the electron trajectory and to the pattern of photon emission and conversions, are used to classify electrons. Class-dependent electron energy measurement errors and identification performances are considered. The tracker and ECAL information are combined for the electron energy measurement at low $p_T^{\rm e}$ and an error estimate is available for each reconstructed electron [24].

4 Data Reduction

The events of interest for the Higgs boson search in the $\rm H \rightarrow 4e$ channel must satisfy a minimal set of requirements. A first and compulsory condition for the events is to satisfy the CMS Level 1 (hardware) trigger (L1) conditions and the filtering of the High Level (software) trigger (HLT). This triggering step is described in Section 4.1. The basic electron triggers are expected to be saturated by SM processes such as the single Z and W production. Further data reduction is obtained with a minimal set of additional electron requirements for a multi-lepton final state as described in Section 4.2. These pre-selection requirements are designed to tame possible background sources involving "fake" electron contamination from QCD jets. They must preserve the signal acceptance, and especially the electron reconstruction efficiency, until later stages where the analysis can best profit from more evolved algorithms applied to reduced event samples.

4.1 Triggering

The events must have satisfied the L1 and HLT trigger requirements corresponding to a *single e* or a *double e* or a *double relaxed e*, as defined in Refs. [28][29]. The *single e* trigger requires one isolated (charged) "electromagnetic" candidate with a threshold set at a reconstructed transverse energy in the ECAL of $E_T = 26.0$ GeV. The *double e* trigger requires two isolated (charged) "electromagnetic" candidates above thresholds of $E_T = 14.5$ GeV. In contrast, the *double relaxed e* trigger does not impose isolation for the (charged) "electromagnetic" candidates and the increased rate is compensated by a higher threshold of $E_T = 21.8$ GeV. The trigger efficiency for the Higgs boson signal as a function of $m_{\rm H}$ and for the main SM backgrounds is shown in Fig. 2.

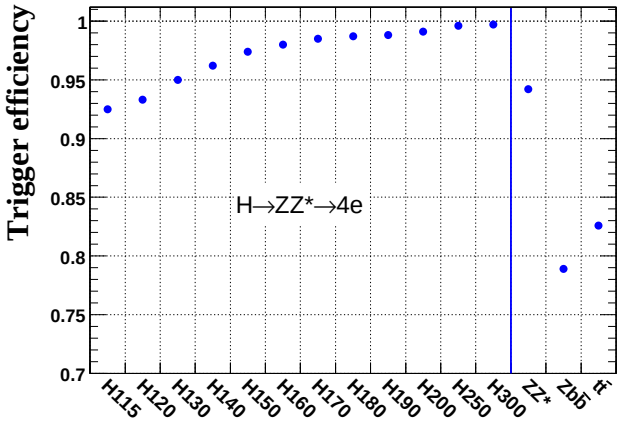

Figure 2: Electron trigger efficiency from the combination of L1 hardware trigger and HLT software trigger in CMS. The efficiency is shown for SM Higgs bosons for various mass hypotheses as well as for the main background processes.

The efficiency is above 95% for $m_{\rm H} > 130$ GeV$/c^2$. Here, only the background sources which are susceptible to fulfill the $\rm 4e$ channel requirements are shown. More details on absolute electron and photon trigger rates can be found in Ref. [30].

4.2 Pre-selection of Four Electron Candidates

Following the L1 and HLT filtering steps, the event candidates must satisfy basic electron pre-selection requirements.

The pre-selection of the signal event candidates relies on the presence of at least 2 e^+ and 2 e^- reconstructed candidates within the acceptance $|\eta| < 2.5$ and with $p_T > 5$ GeV/c, satisfying the following criteria:

- $E_{sc}/p_{in} < 3$, where E_{sc} is the supercluster energy and p_{in} the track momentum at the interaction vertex,
- $|\Delta\eta_{in}| = |\eta_{sc} - \eta_{in}^{extrap.}| < 0.02$, where η_{sc} is the energy weighted position in η of the supercluster and $\eta_{in}^{extrap.}$ is the position in η extrapolated to the ECAL from the track position at vertex and assuming a perfect helix,
- $|\Delta\phi_{in}| = |\phi_{sc} - \phi_{in}^{extrap.}| < 0.1$, where $\Delta\phi_{in}$ is a similar quantity in azimuthal coordinates,
- $H/E < 0.2$, where H is the energy deposited in the HCAL tower just behind the electromagnetic seed cluster and E the energy of the electromagnetic seed cluster,
- and $\sum p_T^{tracks}/p_T^e < 0.5$, a loose track isolation requirement, whose calculation is described in detail in Section 5.1.2.

The electron pre-selection efficiency is shown in Fig. 3 as a function of p_T^e and η^e for the electrons from Higgs boson events at $m_H = 150$ GeV/c^2. The efficiency steeply rises and reaches a plateau around 86% for $p_T^e \gtrsim 20$ GeV/c, is above 90% for $|\eta^e| \lesssim 1.1$ and decreases towards the edge of the tracker acceptance when approaching $|\eta^e| \simeq 2.5$. The pre-selection efficiency for electrons from the same sample is represented in Fig. 3c as a two-dimensional map in the p_T^e versus η^e plane.

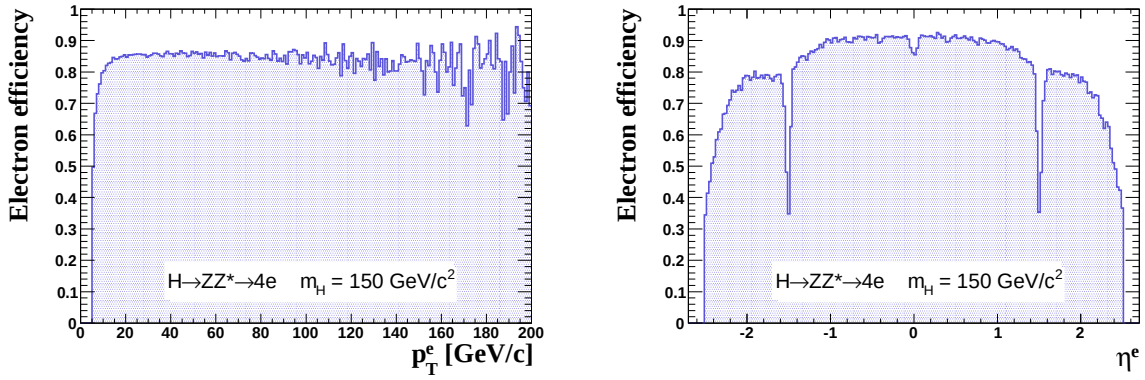

(a) (b)

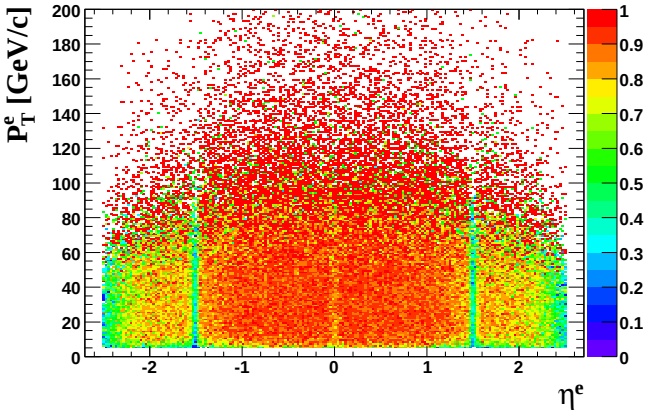

(c)

Figure 3: Pre-selection efficiency for electrons of the $H \to ZZ^{(*)} \to 4e$ channel for $m_H = 150$ GeV/c^2: a) versus p_T^e; b) versus η^e; c) in the p_T^e versus η^e plane.

4.3 Data After Triggering and Pre-selection

The global efficiencies after triggering and multi-electron pre-selection steps are shown in Fig. 4 for the Higgs boson signal at different m_{H} values and for the various $4\mathrm{e}$ backgrounds.

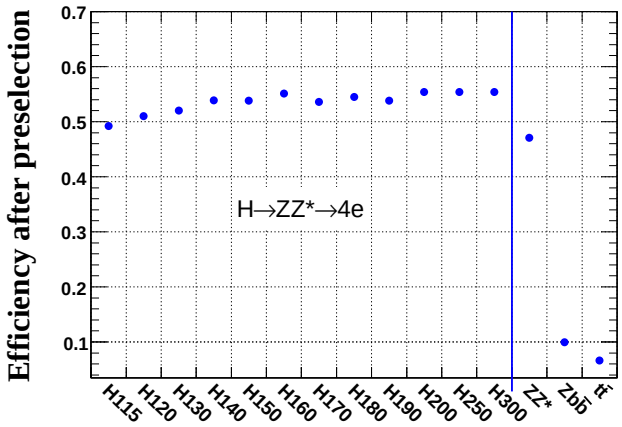

Figure 4: Higgs boson signal and dominant background sources after the triggering and pre-selection steps; the global efficiencies are given for various m_{H} values in the range from 115 to 300 GeV$/c^2$ and for the background from $\mathrm{ZZ}^{(*)}$, $\mathrm{Zb\bar{b}}$ and $\mathrm{t\bar{t}}$.

The acceptance for the Higgs boson signal is maintained above 50% in the full relevant mass range, while the reducible $\mathrm{t\bar{t}}$ and $\mathrm{Zb\bar{b}}$ backgrounds are suppressed by a factor $\gtrsim 10$.

The reconstructed invariant mass $m_{4\mathrm{e}}$ spectrum for signal and background events fulfilling the pre-selection is shown in Fig. 5.

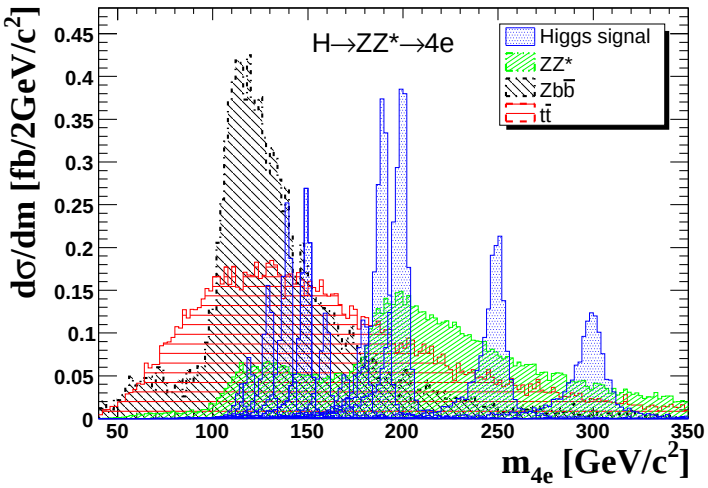

Figure 5: Higgs boson signal and dominant backgrounds contributions to the reconstructed invariant mass $m_{4\mathrm{e}}$ spectrum, after the triggering and pre-selection steps.

A Higgs boson signal could be visible above the background already after data reduction from triggering and pre-selection steps, for masses m_{H} around 150 GeV$/c^2$ or above $\simeq 2m_{\mathrm{Z}}$. More background suppression is clearly required elsewhere.

5 Selection and Kinematics

The next steps of the event selection rely on a more detailed characterization of the electron candidates and on basic kinematic properties of the $\mathrm{H} \to \mathrm{ZZ}^{(*)} \to 4\mathrm{e}$ decay chain.

The sequence of cuts and the choice of observables described in the following for the event selection are largely dictated by the implicit strategy for the discovery in CMS. If the SM Higgs boson is first observed in the $4\mathrm{l}^{\pm}$ channels, then the discovery will have to rely on a statistical observation, involving a small number of events.

Once the existence of a new resonance in the $4l^{\pm}$ channel will have been established at a given m_{H}, the next question will be that of the compatibility with SM expectations, in a first stage by measuring its cross-section, and in a second stage by evaluating its spin and CP quantum numbers. The cuts are chosen here to maximize the significance for an early discovery while preserving the phase space for more involved characterization, e.g. via angular correlations, of the Higgs boson. For the Higgs boson channel in consideration here, this strategy is concomitant with the further suppression of the background sources which involves secondary (or fake) electrons.

5.1 Electron Selection

5.1.1 Vertex Requirements

The electrons from the Higgs boson signal originate from a common primary vertex in contrast to the electrons from at least one $\mathrm{e^+e^-}$ pair reconstructed in $\mathrm{t\bar{t}}$ and $\mathrm{Zb\bar{b}}$ background events. This information is exploited to further improve the separation of the signal and background events. Requirements are imposed on both the longitudinal (IP_L) and the transverse (IP_T) electron impact parameters.

A loose vertex constraint is firstly imposed on the longitudinal impact parameter for the four electron candidates in each event. Each electron is required to satisfy $IP_L/\sigma_L < 13$, where σ_L is the uncertainty (typically $20\ \mu$m for primary tracks) on IP_L.

A more stringent requirement is imposed on the transverse impact parameter to further suppress electrons coming from secondary vertices. Secondary electrons come for instance from semi-leptonic decays subsequent to the hadronization of the b quarks in $\mathrm{Zb\bar{b}}$ and $\mathrm{t\bar{t}}$ background events. For both of these background sources, the displaced vertices will most likely appear in the softest pair of reconstructed electrons. The individual transverse impact parameter significances IP_T/σ_T (where σ_T is the uncertainty on IP_T) are summed up within $\mathrm{e^+e^-}$ pairs. The first (second) pair has its invariant mass the closest (next-to-closest) to the nominal Z boson mass m_{Z}. These $IP_T/\sigma_T^{\mathrm{e}^+} + IP_T/\sigma_T^{\mathrm{e}^-}$ sums are shown separately in Fig. 6.

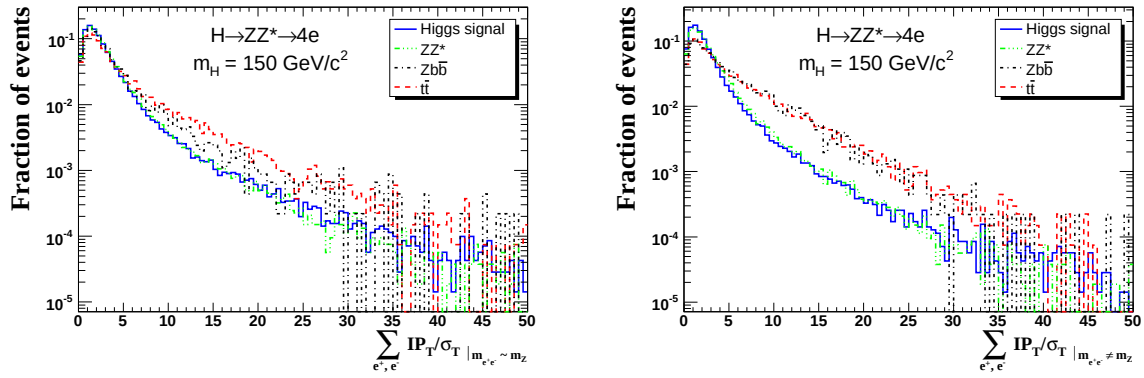

(a) (b)

Figure 6: Sum of the transverse impact parameter significances (IP_T/σ_T) of $\mathrm{e^+e^-}$ pairs for a Higgs boson at $m_{\mathrm{H}} = 150\ \mathrm{GeV}/c^2$, for $\mathrm{ZZ}^{(*)}$, and for $\mathrm{Zb\bar{b}}$ and $\mathrm{t\bar{t}}$; a) $\sum IP_T/\sigma_T$ from the $\mathrm{e^+e^-}$ pair with a reconstructed mass $m_{\mathrm{e^+e^-}}$ best matching the Z boson mass; b) $\sum IP_T/\sigma_T$ from the second $\mathrm{e^+e^-}$ pair.

The $\mathrm{e^+e^-}$ pair with $m_{\mathrm{e^+e^-}} \simeq m_{\mathrm{Z}}$ is requested to have $\sum IP_T/\sigma_T < 30$ while for the other pair the cut is set at 15.

The vertex requirements suppress the $\mathrm{Zb\bar{b}}$ and $\mathrm{t\bar{t}}$ reducible backgrounds by about a factor 2, for an efficiency loss below 8% for the Higgs boson signal and $\mathrm{ZZ}^{(*)}$ background.

5.1.2 Isolation

Electrons from decays of Z or Z^* in the signal are isolated, while electrons coming from b decays in the $\mathrm{t\bar{t}}$ or $\mathrm{Zb\bar{b}}$ backgrounds, located inside a jet, are not isolated. Two partly complementary observables can be best used for the isolation of electrons. These rely either on measurements of primary tracks or on the energy flow in the hadronic calorimeter (HCAL). Both observables are insensitive to the eventual electron-induced electromagnetic showering in the tracker material.

Track Isolation

An isolation cone of size $R_{\rm cone} = \sqrt{\Delta\eta^2 + \Delta\phi^2}$ is defined around the electron direction. Within this isolation cone, reconstructed tracks, other than the candidate electron track, originating from the same vertex as the candidate electron and satisfying $p_T > 1.5$ GeV$/c$ are considered. Other electron tracks inside the cone are not considered if they have a charge opposite to the leading electron charge and if the resulting invariant mass satisfies $m_{\rm e^+e^-} > 10$ GeV$/c^2$. The isolation requirement is imposed on the transverse momentum sum of the considered tracks divided by the electron transverse momentum, $\sum p_T^{\rm tracks}/p_T^{\rm e}$.

Figure 7a shows the isolation efficiency for the Higgs boson signal at $m_{\rm H} = 150$ GeV$/c^2$ as a function of $\rm t\bar{t}$ rejection for different cone sizes $R_{\rm cone}$.

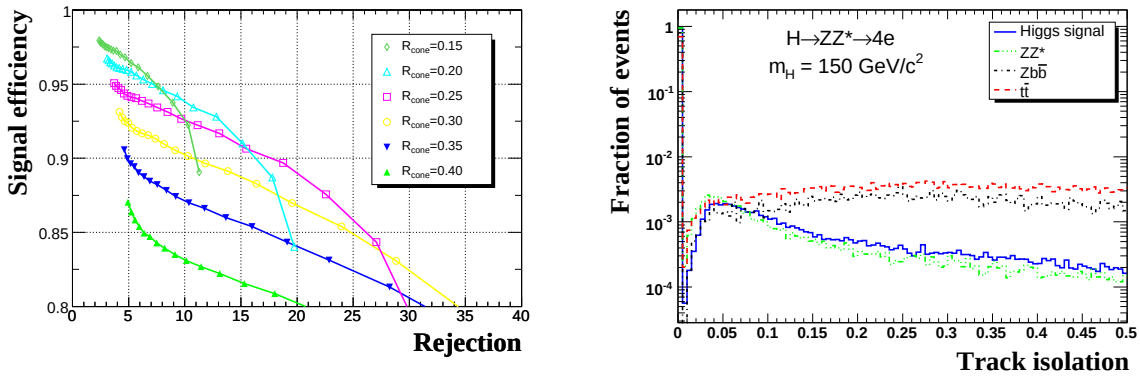

(a) (b)

Figure 7: a) Signal efficiency as a function of the $\rm t\bar{t}$ rejection for different cone sizes, for event samples at pre-selection level; b) track isolation $\sum p_T^{\rm tracks}/p_T^{\rm e}$, for the signal at $m_{\rm H} = 150$ GeV$/c^2$ and for the backgrounds for a cone size $R_{\rm cone} = 0.2$, for event samples after triggering, pre-selection and vertex requirements.

A value $R_{\rm cone} = 0.2$ is chosen as the working point. This value gives a best $\rm t\bar{t}$ rejection for signal efficiency between 90 and 95%. Figure 7b shows the distribution of the track isolation observable $\sum p_T^{\rm tracks}/p_T^{\rm e}$ for the signal at $m_{\rm H} = 150$ GeV$/c^2$ and for the backgrounds.

All the four electrons must satisfy $\sum p_T^{\rm tracks}/p_T^{\rm e} < 0.1$. This electron isolation provides a further suppression, at this stage of the event selection sequence, of more than a factor 2 on the $\rm Zb\bar{b}$ background and about a factor 5 on the $\rm t\bar{t}$ background.

Hadronic Isolation

Within the chosen track isolation cone of size $R_{\rm cone} = \sqrt{\Delta\eta^2 + \Delta\phi^2} = 0.2$, all hadronic calorimeter towers satisfying $E_T > 0.5$ GeV are considered. The hadronic isolation requirement is imposed on the transverse momentum sum of the considered HCAL towers divided by the electron transverse momentum. Figure 8a shows the distributions of the hadronic isolation $\sum E_T^{\rm HCAL}/p_T^{\rm e}$, for the electron which is found to be the least isolated, for the Higgs boson signal at $m_{\rm H} = 150$ GeV$/c^2$ and for the backgrounds. Figure 8b shows similar distributions for the next-to-least isolated electron.

The selection requires that at least three electrons satisfy $\sum E_T^{\rm HCAL}/p_T^{\rm e} < 0.05$, while the least isolated electron is allowed to satisfy a relaxed cut of $\sum E_T^{\rm HCAL}/p_T^{\rm e} < 0.2$. This hadronic isolation further suppresses the $\rm Zb\bar{b}$ background by about 22% and the $\rm t\bar{t}$ background by about 40%, for a signal acceptance $> 95\%$.

5.1.3 Identification

Further electron identification requirements must be imposed to suppress the possible background, involving "fake" electrons, from Drell-Yan processes at NLO where a $\rm Z^{(*)}$ recoils against jet(s). The following discriminating variables are used:

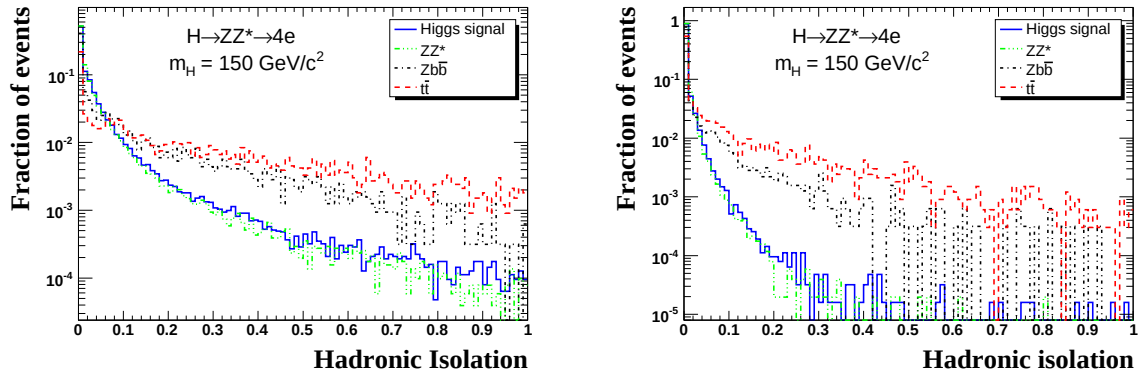

(a) (b)

Figure 8: Hadronic isolation $\sum E_T^{\mathrm{HCAL}}/p_T^{\mathrm{e}}$ for a) the least and b) next-to-least isolated electrons, for the signal at $m_{\mathrm{H}} = 150$ GeV/c^2 and for the backgrounds.

- $\Delta\eta_{\mathrm{in}}$,
- $\Delta\phi_{\mathrm{in}}$,
- H/E,
- $\sum_9 / \sum_{25}$, the ratio of the energy sums over 3×3 and 5×5 crystal matrices centered on the highest energy crystal of the seed cluster,
- $E_{\mathrm{seed}}/p_{\mathrm{out}}$, the ratio of the electromagnetic seed cluster energy over the track momentum at the outermost layer.

Different electron identification cuts are used depending on the distinct classes of track-supercluster electron patterns in order to preserve the electron detection efficiency at all η, and optimize the rejection of fake electrons. The proportions of electrons classes are almost the same for $\mathrm{ZZ}^{(*)}$, $\mathrm{t\bar{t}}$, $\mathrm{Zb\bar{b}}$ backgrounds and for signal, as shown in Table 2, and do not change significantly with cuts. This is due to the fact that these backgrounds have real electrons. On the opposite, a jet faking an electron will have similar characteristics as a showering electron [24]. Therefore class-dependent electron identification cuts are applied to reject fake electrons. They are listed in Table 3 for *golden* and *showering* electrons, separately for the barrel and the endcaps.

	Golden	*Narrow*	*Big Brem*	*Showering*
Signal	22.0%	4.4%	8.7%	54.5%
$\mathrm{ZZ}^{(*)}$	21.2%	5.1%	8.5%	55.4%
$\mathrm{t\bar{t}}$	15.4%	2.8%	5.5%	65.5%
$\mathrm{Zb\bar{b}}$	18.2%	3.1%	6.7%	62.4%

Table 2: Proportion of electron classes for signal events at $m_{\mathrm{H}} = 150$ GeV/c^2 and for the backgrounds, after triggering and pre-selection. The missing proportions correspond to electrons in the cracks and in the barrel-endcap transition region.

	ECAL barrel		ECAL endcaps	
Cut	*Golden*	*Showering*	*Golden*	*Showering*
$\Delta\eta_{\mathrm{in}}$	0.008	0.009	0.008	0.009
$\Delta\phi_{\mathrm{in}}$	0.06	0.08	0.06	0.09
H/E	0.09	0.12	0.09	0.12
Σ_9/Σ_{25}	0.70	0.50	0.80	0.50
$E_{\mathrm{seed}}/\mathrm{p}_{\mathrm{out}}$	0.6-2.5	0.50-/	0.6-2.5	0.50-/

Table 3: Definition of cuts for electron identification based on classes for electrons in the barrel and in the endcap parts of the ECAL.

5.2 Kinematic Requirements

Taking advantage of the expectation of a narrow resonance in the m_{4e} spectrum, and of the likely presence of a real Z boson in the final state, the selection can be further improved using mass dependent kinematic requirements.

First, the electrons of the e^+e^- pair with the lowest invariant mass have a much harder p_T^e spectrum for the Higgs boson signal than for the $t\bar{t}$ and $Zb\bar{b}$ backgrounds. Second, the mass spectrum of the Z bosons distinguishes the Higgs boson signal from the $ZZ^{(*)}$ background. These kinematic requirements are discussed in the following.

5.2.1 Electron p_T Cuts

The cascade $H \rightarrow ZZ^{(*)} \rightarrow 4e$ for a Higgs boson, mostly produced at small transverse momentum, leads to very characteristic ordered p_T^e spectra for the four final state electrons. Moreover, the p_T^e spectra of the softest electrons for the Higgs boson signal are harder than the ones expected from secondary electrons from the $Zb\bar{b}$ or $t\bar{t}$ backgrounds. Thus, it is advantageous to profit from the knowledge of the expected p_T^e distributions for the Higgs boson signal. An optimum set of p_T^e cuts as a function of m_H is given in Table 4. The cut on the softest electron is maintained to a low and constant value for simplicity and to preserve the signal efficiency at low m_H. Otherwise the p_T^e cuts are slowly evolving for as long as $m_H < 2m_Z$ and then rise faster above the Z pair production threshold.

m_H (GeV/c^2)	p_T^1 (GeV/c)	p_T^2 (GeV/c)	p_T^3 (GeV/c)	p_T^4 (GeV/c)
115	7	10	10	15
120-150	7	12	15	15
160	7	15	15	15
170-180	7	15	15	20
190	7	15	20	30
200	7	15	25	30
250	7	20	40	50
300	7	30	40	60

Table 4: Electron p_T cuts for different Higgs mass hypothesis, from the lowest to the highest p_T electron.

5.2.2 Invariant Mass Requirements

Labelling Z_1 (Z_2) the e^+e^- pair reconstructed with an invariant mass $m_{e^+e^-}$ the closest (next-to-closest) to the nominal Z mass, one expects for $m_{4e} < 2m_Z$ in the case of the Higgs boson signal that $m_{4e} \simeq m_{Z_1} + m_{Z_2}$ with most often the presence of a Z boson on its mass shell, $m_{Z_1} \simeq m_Z$. The Z boson masses saturate the phase space and the vector bosons are dominantly produced with small velocity in the Higgs boson rest frame. The requirement of one real Z boson further suppresses the $t\bar{t}$ backgrounds for low m_H. The cut on Z_2 is powerful against the $ZZ^{(*)}$ continuum and further suppresses the $Zb\bar{b}$ and $t\bar{t}$ backgrounds. A set of optimal Z_1 and Z_2 mass cuts is given in Table 5.

m_H (GeV/c^2)	$m_{Z_1}^{min}$ (GeV/c^2)	$m_{Z_1}^{max}$ (GeV/c^2)	$m_{Z_2}^{min}$ (GeV/c^2)	$m_{Z_2}^{max}$ (GeV/c^2)
115-120	51	101	10	50
130	61	101	10	60
140	71	101	10	65
150	71	101	15	65
160	71	101	15	70
170	81	101	20	80
180	81	101	30	90
190	81	101	40	100
200	81	101	40	110
250	51	131	20	200
300	51	131	15	300

Table 5: Invariant mass cuts on the reconstructed Z_1 and Z_2 bosons.

The lower bound on the Z_1 mass acceptance window decreases at small m_H values to take into account the development of a low mass tail due to the increasing Z^*Z^* contribution. The width of the acceptance mass windows

for both Z_1 and Z_2 is increased towards large m_H values where the reducible backgrounds have contributions already negligible after the p_T^e cuts.

5.3 Event Selection Summary

A summary of the selection efficiencies for the Higgs boson signal and backgrounds after each sequential step of the analysis is presented in Tables 6 and 7.

m_H (GeV/c^2) :	115	120	130	140	150	160	170	180	190	200	250	300
L1 and High Level Trigger												
Signal	92.5	93.3	95.0	96.2	97.4	98.0	98.5	98.7	98.8	99.1	99.6	99.7
$ZZ^{(*)}$						⟵	94.2	⟶				
$Zb\bar{b}$						⟵	78.9	⟶				
$t\bar{t}$						⟵	82.7	⟶				
Pre-selection												
Signal	53.2	54.6	54.8	56.0	55.2	56.2	54.4	55.2	54.4	55.9	55.7	55.6
$ZZ^{(*)}$						⟵	50.0	⟶				
$Zb\bar{b}$						⟵	12.6	⟶				
$t\bar{t}$						⟵	8.0	⟶				
Vertex Impact Parameter												
Signal	94.0	93.5	94.5	94.6	94.0	93.8	93.9	94.1	93.8	92.8	93.2	93.0
$ZZ^{(*)}$						⟵	93.6	⟶				
$Zb\bar{b}$						⟵	54.9	⟶				
$t\bar{t}$						⟵	42.6	⟶				
Track Isolation												
Signal	91.5	91.2	91.7	91.9	92.3	93.2	93.5	94.1	93.9	94.3	94.8	94.9
$ZZ^{(*)}$						⟵	93.4	⟶				
$Zb\bar{b}$						⟵	44.8	⟶				
$t\bar{t}$						⟵	21.4	⟶				
Hadronic Isolation												
Signal	95.4	95.3	95.2	95.1	95.5	95.7	95.3	95.7	96.0	96.1	96.2	95.6
$ZZ^{(*)}$						⟵	95.9	⟶				
$Zb\bar{b}$						⟵	78.4	⟶				
$t\bar{t}$						⟵	59.6	⟶				
Electron Identification												
Signal	92.4	92.7	93.1	94.6	95.8	95.7	95.7	95.7	96.0	96.1	95.7	95.8
$ZZ^{(*)}$						⟵	95.1	⟶				
$Zb\bar{b}$						⟵	80.8	⟶				
$t\bar{t}$						⟵	77.6	⟶				

Table 6: Summary of event selection efficiencies (in %) for the triggering, pre-selection and electron selection steps of the analysis; the efficiencies are given at each step relative to the previous selection step in the sequence, for the different signal samples and for the SM backgrounds.

For any of the Higgs boson mass hypotheses, the dominant remaining background after all the cuts is the $ZZ^{(*)}$ continuum which amounts to $> 75\%$ of the total background over the full mass range and to $> 97\%$ for $m_H \geq 2 \times m_Z$. The $Zb\bar{b}$ background contribution decreases from 20-15% at low masses to $< 2\%$ for $m_H \geq 2 \times m_Z$. The $t\bar{t}$ background remains small for the whole mass range: $\sim 7\%$ for $m_H = 115, 120$ GeV/c^2, $< 5\%$ for 130 GeV/$c^2 \leq m_H \leq$ 170 GeV/c^2 and $< 0.6\%$ for $m_H \geq 2 \times m_Z$. Figure 9 presents the m_{4e} invariant mass distributions for the signal at $m_H = 150$ GeV/c^2 and for the backgrounds just after the trigger and pre-selection requirements, and after all cuts.

5.4 Measurements and Control of Background Rates

Following the electron selection (Section 5.1) and the application of basic kinematic requirements (Section 5.2), the $ZZ^{(*)}$ background remains as the dominant or sole background over the full mass range in consideration for the SM Higgs boson search in this channel. The requirement that one of the e^+e^- pairs gives an invariant mass $m_{e^+e^-}$ compatible with the presence of a real Z boson in the final state together with electron isolation has helped to considerably suppress the $t\bar{t}$ background. The primary vertex requirements for the second e^+e^- pair of isolated

m_{H} (GeV/c^2) :	115	120	130	140	150	160	170	180	190	200	250	300
						Electron p_T cuts						
Signal	75.1	75.2	84.8	90.2	93.2	93.3	96.0	97.7	97.5	97.8	91.6	86.1
$ZZ^{(*)}$	91.5	90.1	90.1	90.1	90.1	87.5	87.4	87.4	86.5	85.4	61.1	37.7
$Zb\bar{b}$	26.9	19.0	19.0	19.0	19.0	10.8	10.8	10.8	10.0	8.3	0.98	0.08
$t\bar{t}$	37.5	29.6	29.6	29.6	29.6	20.1	20.1	20.1	18.4	15.6	4.9	2.1
						Invariant Z_1 mass						
Signal	96.0	98.3	96.3	94.3	96.5	97.0	98.0	96.6	98.7	99.1	100	100
$ZZ^{(*)}$	98.5	98.6	98.3	97.7	97.7	98.0	98.0	96.5	96.9	97.2	99.9	99.9
$Zb\bar{b}$	91.8	93.1	90.9	90.9	90.9	93.9	93.9	87.1	90.2	91.1	100	100
$t\bar{t}$	80.8	83.3	72.8	54.7	54.7	57.8	57.8	39.4	41.3	43.7	99.2	98.1
						Invariant Z_2 mass						
Signal	90.4	91.5	95.7	98.1	93.8	93.7	94.3	95.7	97.4	97.8	99.7	100
$ZZ^{(*)}$	15.5	14.8	17.1	18.0	15.5	16.2	21.3	56.2	79.6	84.0	97.1	98.5
$Zb\bar{b}$	56.3	59.7	63.0	64.9	60.2	64.5	61.3	46.1	26.4	26.1	83.3	100
$t\bar{t}$	63.6	63.6	72.4	73.4	70.3	68.3	66.3	50.7	37.1	41.6	97.7	100
						Global Efficiency						
Signal	24.3	26.0	31.2	35.2	36.0	37.4	38.0	39.9	40.9	42.5	41.2	38.6
$ZZ^{(*)}$	5.24	4.94	5.68	5.95	5.14	5.23	6.87	17.8	25.1	26.2	22.3	13.9
$Zb\bar{b}$	0.22	0.16	0.17	0.17	0.16	0.10	0.097	0.068	0.037	0.031	0.013	0.001
$t\bar{t}$	0.054	0.044	0.043	0.033	0.032	0.022	0.021	0.011	0.008	0.008	0.013	0.006

Table 7: Summary of event selection efficiencies (in %) for the kinematic requirements; the efficiencies are given at each step relative to the previous selection step in the sequence, for a Higgs boson signal at a mass m_{H} and for the SM backgrounds. Global efficiency with respect to the generator pre-selection is also shown.

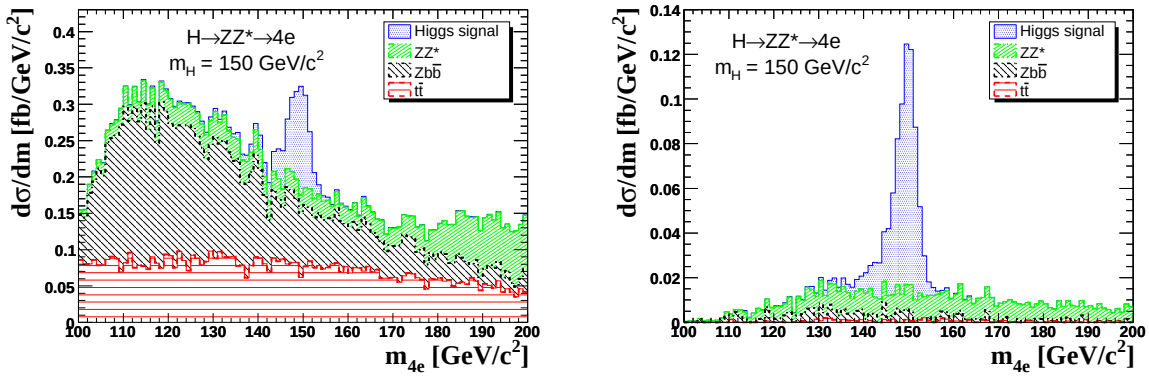

(a) (b)

Figure 9: Distributions of the reconstructed invariant mass $m_{4\mathrm{e}}$ for the SM Higgs boson signal at $m_{\mathrm{H}} = 150$ GeV/c^2 and for the SM backgrounds a) after the trigger and pre-selection requirements and b) after all cuts. The distributions are normalized in cross-section.

electrons has helped rejecting the $Zb\bar{b}$ background. Thus, the determination of the mean expected number of $ZZ^{(*)}$ background events in the signal region, defined e.g. by a simple sliding window in the $m_{4\mathrm{e}}$ spectrum, remains as the key issue.

There are three methods for the estimation of the $ZZ^{(*)}$ contribution to the background in the signal region:

- a direct simulation of the $ZZ^{(*)} \rightarrow 4\mathrm{e}$ process,
- a normalization to the $Z \rightarrow \mathrm{e}^+\mathrm{e}^-$ data,
- a normalization to the sidebands.

The first method entirely relies on existing SM constraints and the theoretical knowledge, with uncertainties coming from the PDFs used to describe the colliding protons and from QCD scale variations. It furthermore relies on the LHC luminosity measurements, and on the Monte Carlo (MC) modelling of the acceptance and detector response for what concerns the uncertainties arising from electron reconstruction and selection. Otherwise, the

method benefits from the fact that the statistical precision on the mean background expectation is only limited by the MC statistics, and can therefore be assumed negligible in the context of a prospective for an analysis to be carried in the CMS experiment.

The second method (henceforward referred to as the ZZ/Z method) aims at profiting from the fact that the SM single Z production cross-sections will have been measured with a great precision by the time the LHC reaches an integrated luminosity of $\mathcal{O}(10)$ fb^{-1}. As a figure of merit, the CDF experiment at the Tevatron $p\bar{p}$ collider has measured the $\sigma_{\gamma^*/\mathrm{Z}} \times BR(\gamma^*/\mathrm{Z} \to \mathrm{l}^+\mathrm{l}^-)$ with statistical and systematic uncertainties of 1.3% and 1.8% respectively, at 72.0 ± 4.3 pb^{-1} integrated luminosity [31]. Using a ratio of $\mathrm{ZZ}^{(*)} \to \mathrm{e}^+\mathrm{e}^-\mathrm{e}^+\mathrm{e}^-$ to $\mathrm{Z} \to \mathrm{e}^+\mathrm{e}^-$ rates allows one to profit from a full cancelation of pp luminosity uncertainties, while providing a partial cancelation of PDF and QCD scale variations uncertainties (due to their correlations in a part of the initial state phase space) and a partial cancelation of experimental uncertainties.

In the third method, the normalization to the sidebands, the number of background events in the signal region (N_b^{in}) is determined from the number of observed background events outside the signal region (N_b^{out}) multiplied by the fraction $\alpha(MC)$ of these two values obtained from MC simulation:

$$N_b^{\mathrm{in}} = \frac{N_b^{\mathrm{in}}(MC)}{N_b^{\mathrm{out}}(MC)} \times N_b^{\mathrm{out}} = \alpha(MC) \times N_b^{\mathrm{out}}. \quad (1)$$

Using the sidebands one also expects to fully cancel luminosity uncertainties, to reduce PDF and QCD scale variation uncertainties and also to substantially reduce experimental uncertainties. Statistical errors with sidebands normalization come from the statistics of the background rate outside the signal region and can be a limiting factor for the method. By relaxing some of the kinematic cuts, such as the Z invariant mass cut, the background rate outside the signal region increases, reducing therefore the statistical errors for this method. The price to pay is an increased background rate in the signal region too. This is discussed in more details in Section 6.3.

6 Systematics

In this section we discuss systematic errors and distinguish "theoretical" and "experimental" errors. These are discussed here in the context of a discovery via a simple counting method. The theoretical uncertainties concern the estimation of the background rates within the cuts defining the acceptance of the Higgs boson signal. The experimental uncertainties take into account the limited knowledge of the detector responses and efficiencies, and of the corresponding MC modelling.

6.1 Theoretical Errors

The uncertainty on the number of background events in the signal region from PDFs and QCD scales variations has been estimated using the MCFM [17] program. CTEQ6M PDF are used and 20 eigenvector parameters have been varied by $\pm 1\sigma$. Both QCD normalization and factorization scales have been varied independently up and down by a factor two with respect to their nominal values of $2 \times m_{\mathrm{Z}}$. The resulting uncertainties from PDF and QCD scale are of the order of 6% for a direct estimation of the $\mathrm{ZZ}^{(*)}$ background, from 2 to 8% for a normalization to single $\mathrm{Z} \to \mathrm{e}^+\mathrm{e}^-$ (ZZ/Z method) and from 0.5 to 4% for a normalization to sidebands [32]. A 8% uncertainty on the gluon fusion cross-section in the $\mathrm{ZZ}^{(*)}$ background is also considered as a part of the theoretical uncertainties.

The uncertainty on the normalization of the measurements to the pp luminosity of the LHC collider is estimated to be of the order of 3% for an integrated luminosity above 10 fb^{-1}.

6.2 Experimental Errors

An uncertainty of $\pm 1\%$ is estimated on the L1/HLT trigger efficiency. Other sources of experimental systematics are the uncertainties on the tracker material budget, on electron energy and momentum scales and resolutions, and on electron reconstruction efficiencies.

The strategy adopted consists in using single W and Z production which provides electrons via $\mathrm{W} \to \mathrm{e}\nu$ and $\mathrm{Z} \to \mathrm{e}^+\mathrm{e}^-$ decays, to control the energy measurements and reconstruction efficiencies, and then rely on the MC modelling for the extrapolation over the full p_T^{e} and η^{e} ranges relevant for this analysis.

6.2.1 Material Budget

A possibly important source of systematics on electron reconstruction comes from the limited knowledge of the material budget. A change of the integral amount of the tracker material traversed by electrons before reaching the

ECAL is susceptible to affect the electron selection and identification efficiencies, as well as the energy measurement and resolution. The uncertainty on the material budget will limit the precision of the acceptance calculations when using the MC model to extrapolate away from the kinematic domain best constrained via single Z and W measurements.

There are many observables that are directly or indirectly sensitive to the amount of tracker material, and which have been used in collider experiments. Examples are the distribution of converted photon vertices, or the shape of the E/p distribution comparing for electrons the tracker momentum measurement p to the energy E measured in the calorimeter within a finite cluster volume, or a comparison of data and MC for the Z mass resolution, etc.

A new technique can be used based on the electron GSF tracking introduced recently in CMS [24]. The mean fraction $f_{\rm brem}$ (introduced in Section 3) of the energy radiated along the complete trajectory is roughly proportional to the integral amount of traversed material. Hence, one can relate $f_{\rm brem}$ to the material thickness X/X_0 where X_0 is the characteristic radiation length, via the formula $< X > /X_0 \simeq -ln(1 - f_{\rm brem})$. The amount of tracker material measured in this way for single electron data is shown in Fig. 10a.

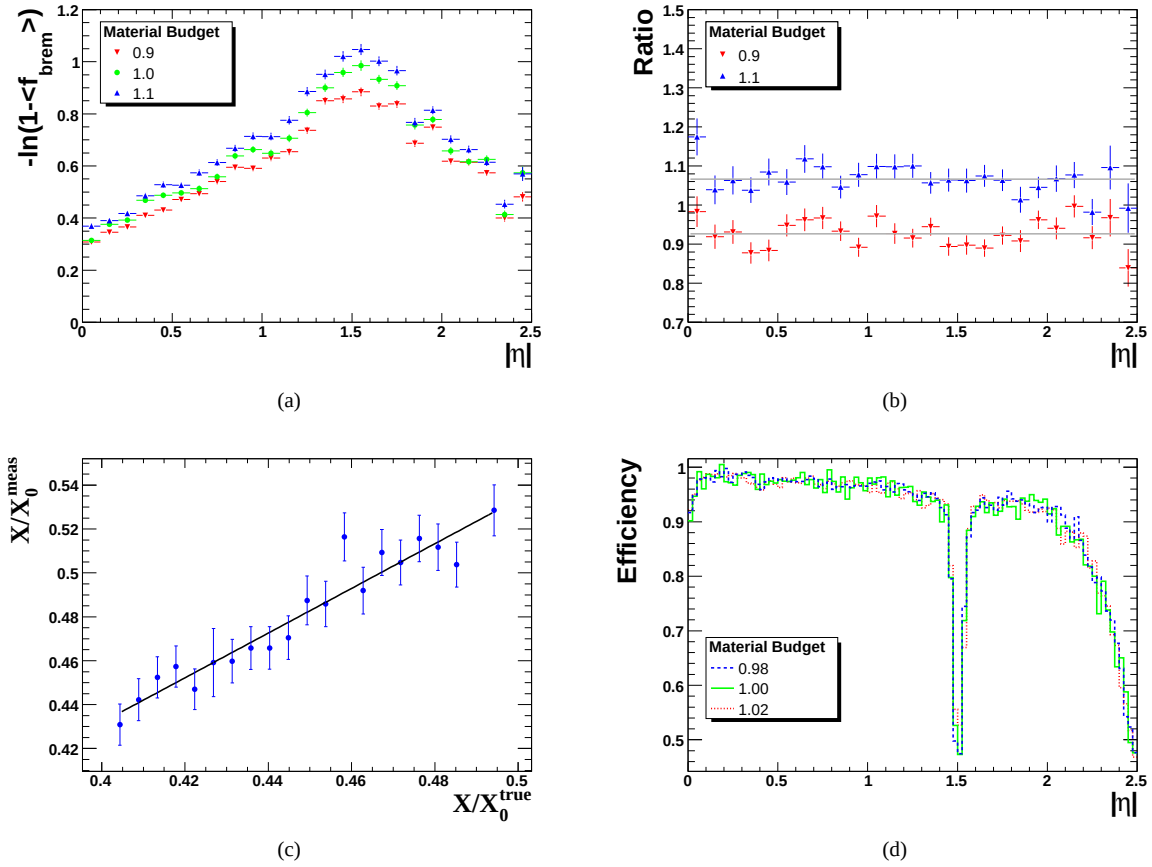

Figure 10: Sensitivity to variations of the tracker material budget from electron measurements based on GSF tracks; a) measured amount of material as a function of $|\eta|$ for the nominal tracker configuration and for an integral material budget changed by $\pm 10\%$; b) ratio of the measured amount of material as a function of $|\eta|$; c) measured versus true thickness in X_0 of the tracker material; d) effect of a change of 2% of the material budget on the electron reconstruction efficiency.

The results obtained in the configuration corresponding to the nominal tracker material coincide very well with the known material distribution as given in Ref. [4]. Figure 10b shows the ratio of the material thickness obtained by the above method to the measurement results in the nominal case, for configurations where the amount of material was changed by $\pm 10\%$. The ratio is found to be remarkably stable as a function of η, despite the fact that the integral amount of material has a strong η dependence. Thus, single electrons can be used in CMS to tune the MC model of the tracker material per η slice.

Figure 10c shows that in a given η slice the material thickness is linearly correlated (at least within a range of $\pm 10\%$) to the true material thickness. Similar results are obtained when considering various restricted ranges of $p_T^{\rm e}$ within a sample of uniformly distributed electrons in the $p_T^{\rm e}$ range from 5 to 100 GeV/c. With the electron

statistics expected from single Z production for an integrated LHC luminosity of $\mathcal{O}(10)$ fb^{-1}, it should be possible to determine the tracker material thickness to a precision better than 2% over the full acceptance in η.

Figure 10d shows that such a 2% uncertainty on the material budget will have almost no effect on the electron reconstruction efficiency uncertainty. A residual effect of the material budget uncertainty is expected in signal and background acceptance, e.g. through fluctuations induced on observables used in the kinematic requirement cuts. As a figure of merit, CDF has estimated an acceptance uncertainty of about 1% in the $Z \rightarrow e^+e^-$ decay channel from a 1.5% (16.5%) uncertainty in material budget description for the central (forward) part of their detector [31].

6.2.2 Control from Data

The electron reconstruction efficiency and energy scale can be controlled by using tagged electrons from $W \rightarrow e\nu$ and $Z \rightarrow e^+e^-$ decays. The huge cross-sections for the single Z and W production at the LHC promise a very significant reduction of reconstruction uncertainties already after an integrated luminosity of a few fb^{-1}. Electrons from $Z \rightarrow e^+e^-$ are produced centrally with a characteristic Jacobian peak for the p_T^e distributions around 45 GeV$/c$. It is therefore expected that the best control of (i.e. smallest) experimental systematics is obtained in the central part of the detector, and for electrons with p_T^e around $m_Z/2$.

The electron reconstruction relies on a classification of electrons sharing common types of observable features and improved (class-dependent) electron identification, energy measurement and error estimations are obtained. A control and fine tuning of the classification can also be performed using $Z \rightarrow e^+e^-$ data [33], as demonstrated in Fig. 11a and in Fig. 11b showing the distribution of electrons versus η and p_T for different classes, together with statistical errors after 0.15 fb^{-1} of collected data.

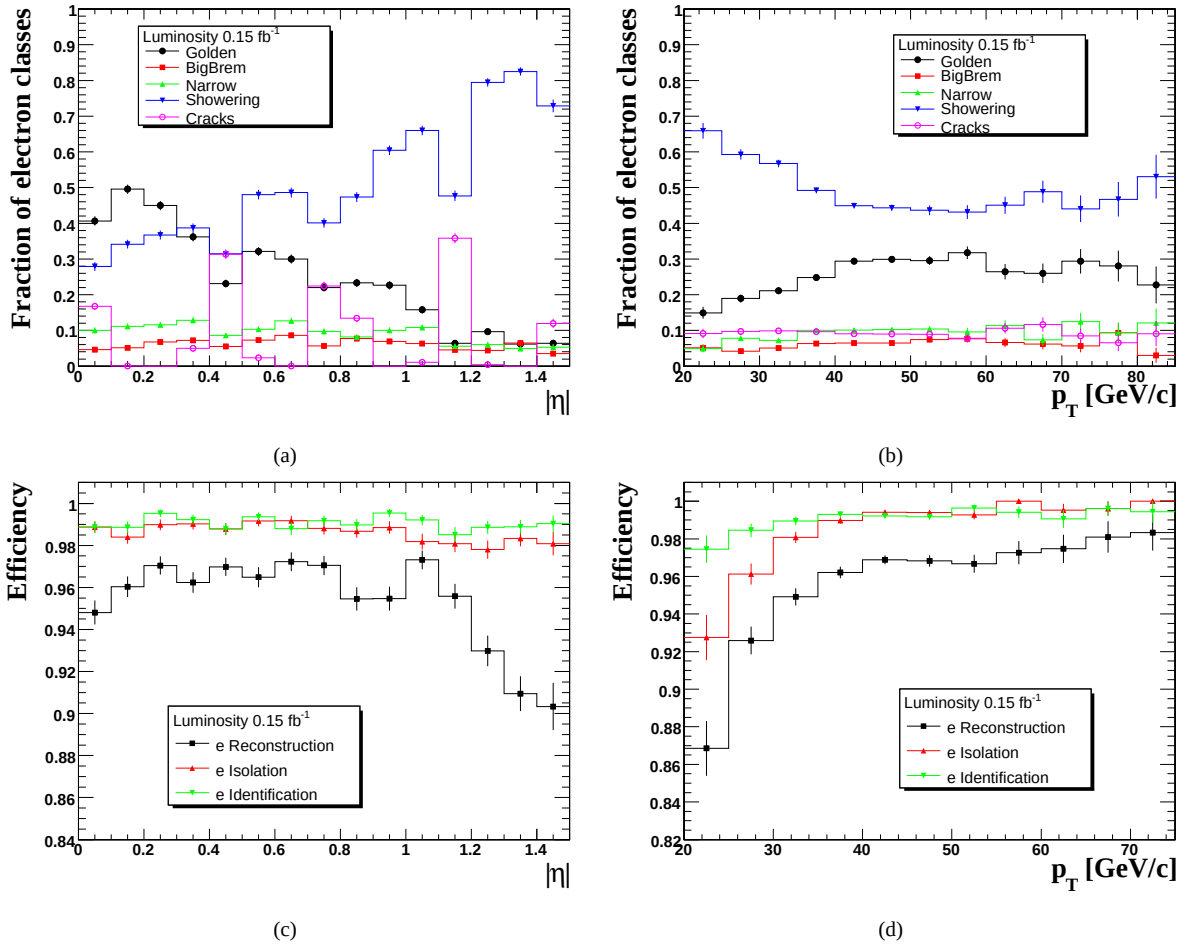

Figure 11: Fraction of electron population in the classes versus a) $|\eta|$ and b) p_T, with statistical errors, for electrons from $Z \rightarrow e^+e^-$ decay. Reconstruction, isolation and identification efficiencies with associated errors as a function of c) $|\eta|$ and d) p_T. Results are for an integrated luminosity of 0.15 fb^{-1}.

The strategy proposed for the control of the reconstruction efficiencies and of the associated systematic uncer-

tainties consists of selecting $Z \rightarrow e^+e^-$ events having at least one leg reconstructed as a *golden* electron. The second leg is then used to estimate reconstruction efficiencies and uncertainties. The electron reconstruction, isolation and identification efficiencies with associated errors as a function of η and p_T are shown in in the η range of the ECAL barrel in Fig. 11c and in Fig. 11d.

The uncertainties on the measurements of the electron reconstruction, isolation, and identification efficiencies are given as a function of η and p_T in Fig. 12, together with the evolution of the error on the reconstruction efficiency with the integrated luminosity. In all plots, increased uncertainties are observed when moving away from the Jacobian peak. Uncertainties in η remain constant over the whole range of the ECAL barrel, except for an increase towards $\eta \approx 1.5$ caused by a drop in the reconstruction efficiency near the transition region. From the size of reconstruction, isolation and identification errors and their evolution with the integrated luminosity, all shown in Fig. 12, one can safely absorb all reconstruction efficiency uncertainties in a single factor of 1% per electron.

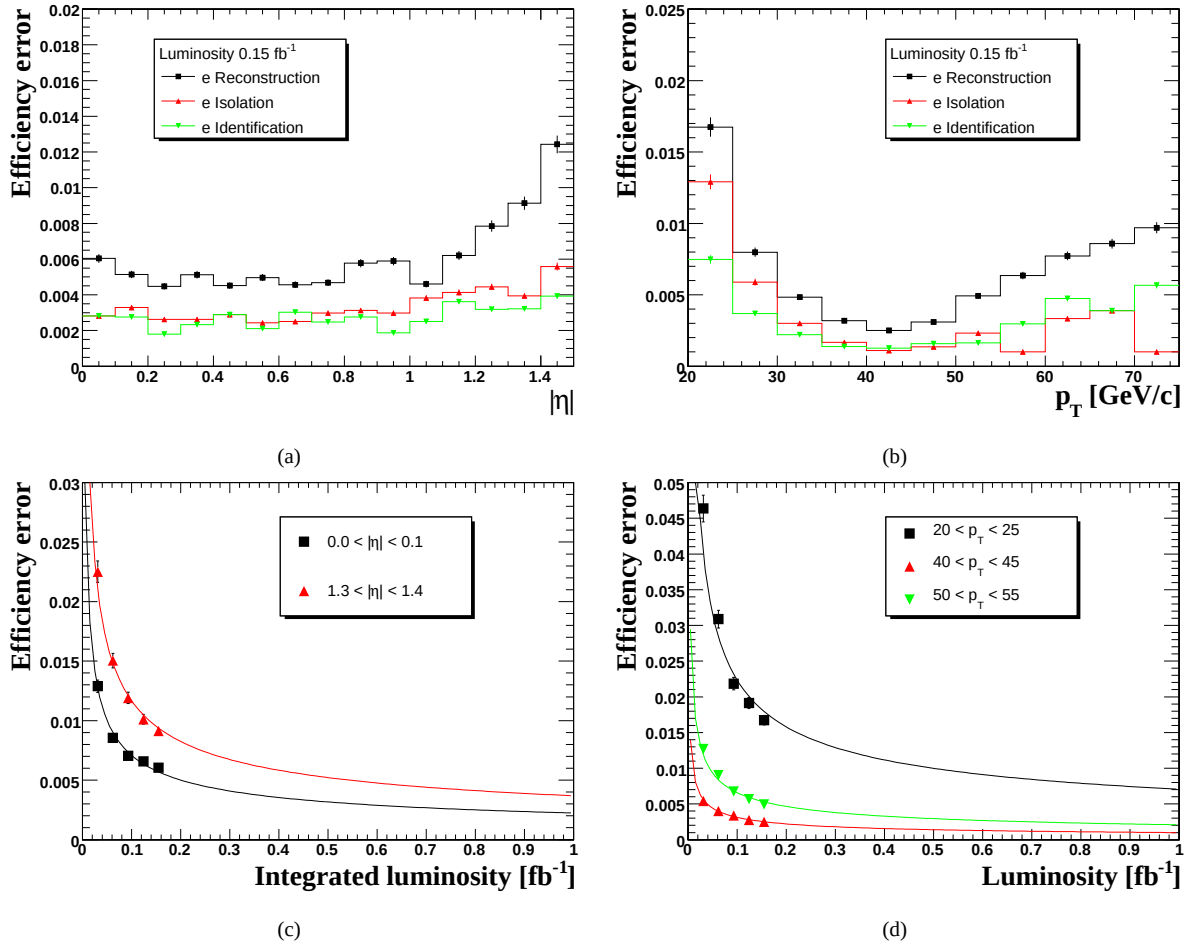

Figure 12: Uncertainties on the measurements of electron reconstruction, isolation and identification efficiencies as a function of a) $|\eta|$ and b) p_T. Evolution of the reconstruction uncertainties with the integrated luminosity in two slices of c) $|\eta|$ and three slices of d) p_T.

The second important systematic effect is the uncertainty on the energy scale determination. In Ref. [33] it has been shown that the average uncertainty on the electron energy scale is expected using single $Z \rightarrow e^+e^-$ data to be of about 0.04% for an integrated luminosity $\gtrsim 0.2$ fb^{-1}. Since electrons from the $H \rightarrow 4e$ decay have different p_T^e spectra, it remains necessary to estimate the systematics expected as a function of the integrated luminosity and over the relevant p_T^e range. For this analysis, a loose constraint on the Z boson mass is combined with stringent electron identification requirements on one decay leg, in order to tag the second leg as a candidate electron. This second leg is then used as a probe to estimate the systematic error on the energy scale. The uncertainties versus η and p_T and their evolution as a function of the expected integrated luminosity are shown in Fig 13. From these results, one can safely estimate the uncertainty on the energy scale to 0.5% in the ECAL barrel region, and 1% in

the ECAL endcaps.

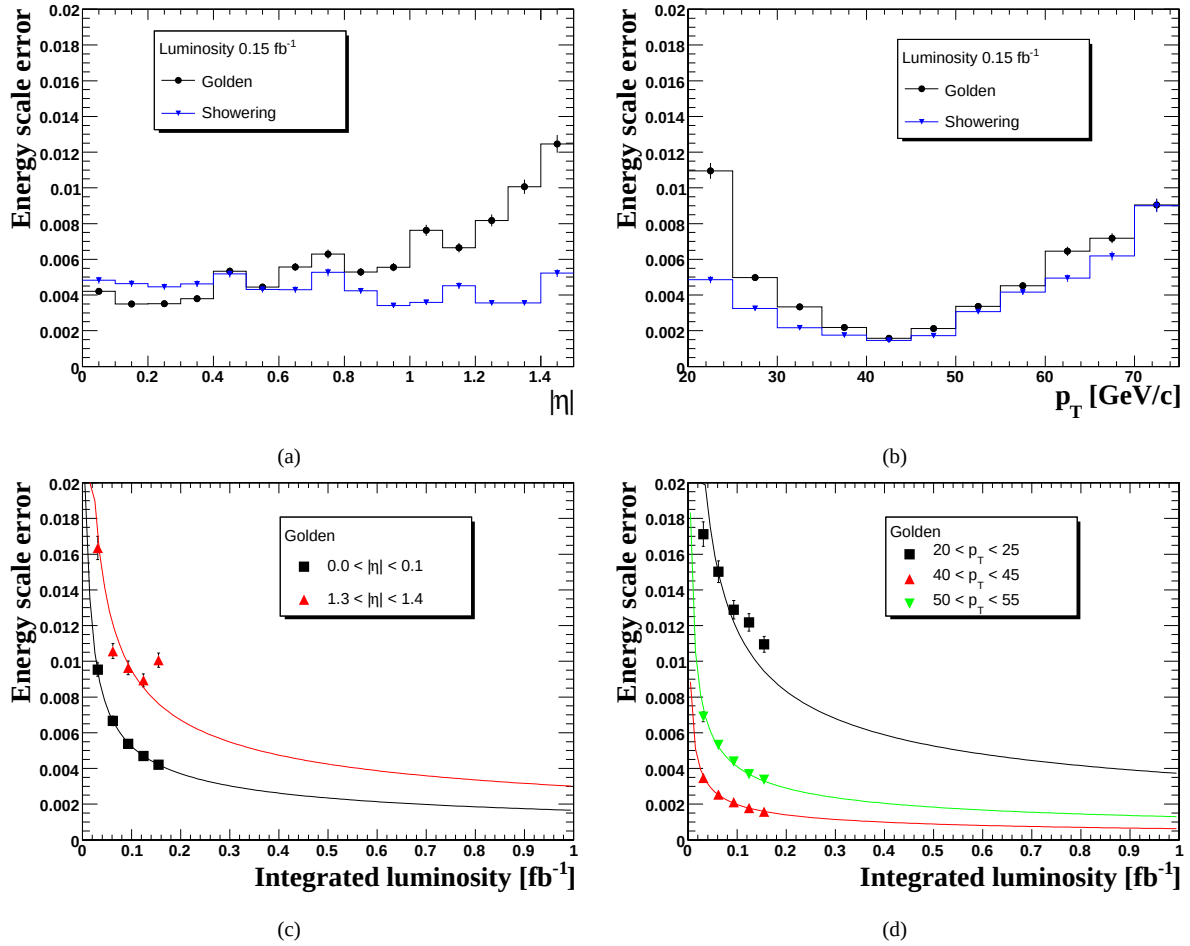

Figure 13: Uncertainties on the energy scale measured from $Z \rightarrow e^+e^-$ for golden and showering electrons as a function of a) $|\eta|$ and b) p_T and their evolution, for the golden electrons, with the integrated luminosity in two slices of c) $|\eta|$ and three slices of d) p_T.

6.3 Comparison of Background Systematics

In this section, the full systematic and statistical uncertainties are evaluated for two methods of background estimation: normalization to the $Z \rightarrow e^+e^-$ measurements and normalization to the sidebands. The theoretical uncertainties from PDF and QCD scale variations have been discussed in the Section 6.1 and results are taken from Ref. [32].

The experimental uncertainties are evaluated by combining quadratically the effects obtained with varying the energy scale, trigger and reconstruction efficiencies by the uncertainties from the previous section. From this, a total uncertainty from the direct simulation on the number of background events in the signal region is about 5%. As expected the uncertainty is reduced when normalizing to the sidebands, to about 2%. As experimental uncertainty for the $Z \rightarrow e^+e^-$ normalization the mean value of these two uncertainties at each mass point is taken.

Both theoretical and experimental systematic uncertainties for the background normalization to single $Z \rightarrow e^+e^-$ measurements are shown in Fig. 14a. The overall systematic uncertainty obtained with this method is about 5%.

The computed uncertainties for the sidebands normalization are shown in Fig. 14b. Statistical uncertainties scale as the square root of the number of background events outside the signal region and are shown for an integrated luminosity of 30 fb^{-1} and for two analysis scenarios: after all analysis cuts where a maximal significance is the main goal, and without cuts on the mass of both Z bosons where statistical errors are reduced by increasing the number of background events. The second method results in a somewhat lower nominal significance (by about

8%) while the statistical errors decrease by a factor of about 2.5.

Based on these results full significance calculations with and without systematics are presented in the following section.

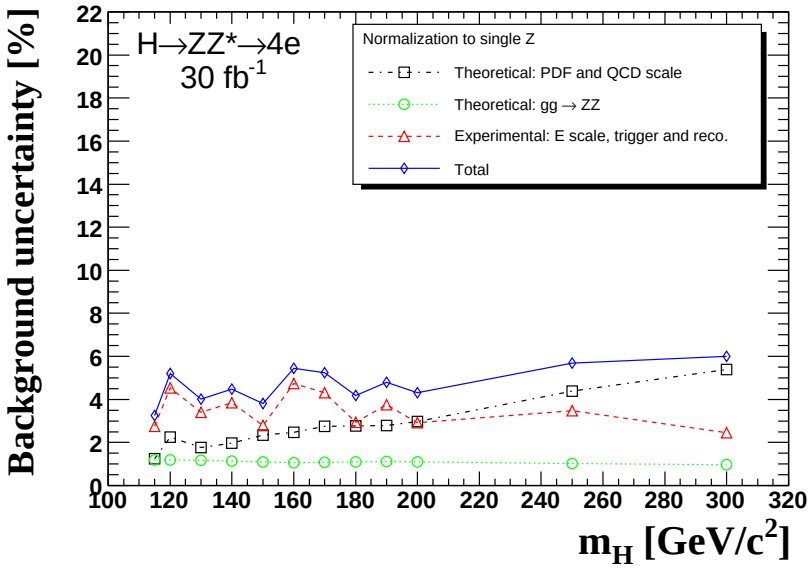

(a)

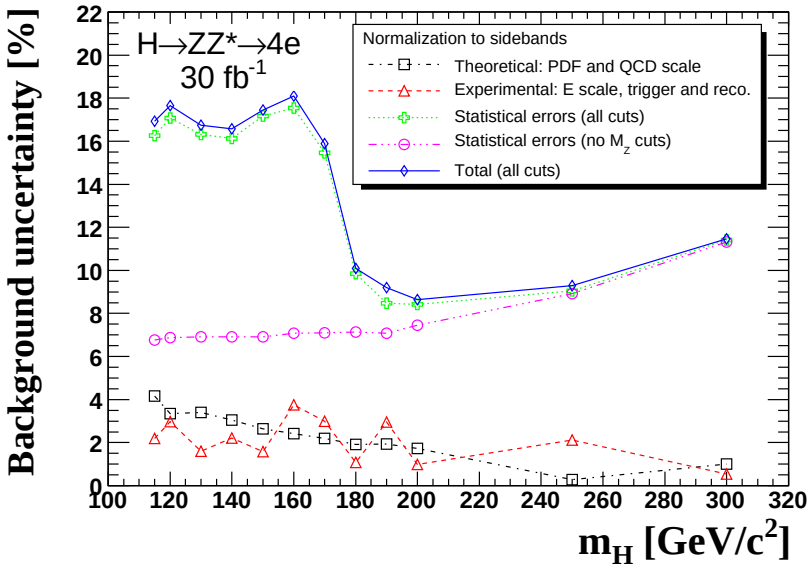

(b)

Figure 14: Theoretical and experimental uncertainties on $ZZ^{(*)}$ background, using two different methods to evaluate background from data: a) normalization to the single $Z \rightarrow e^+e^-$ measurement and b) normalization to the sidebands. Expected statistical errors for sidebands are shown for an integrated luminosity of 30 fb^{-1}.

7 Results

7.1 Observability

A simple counting experiment is used here to quantify the sensitivity of the experiment to the presence of a Higgs boson signal. The expected number of signal (N_s) and background (N_b) events are evaluated in a sliding

window whose central position varies between 100 and 320 GeV/c^2.

The counting experiment significance S_{cP} is defined as the probability from a Poisson distribution with mean N_b to observe a number of events equal or greater than $N_s + N_b$, converted in equivalent number of sigmas of a Gaussian distribution. The systematic errors due to the probability density function knowledge contain in general a contribution from absolute systematic errors and a contribution from statistics (as in the case of the estimation of the background from the sidebands described in Section 6.2.2) and the significance is evaluated following Ref. [34].

As a comparison, the significance results are also given using the widely used log-likelihood ratio (LLR) significance S_{cL}, as proposed in Ref. [35]. This significance estimate is obtained forming the statistical test of the signal+background hypothesis against the background only hypothesis using a likelihood ratio. Assuming a Poisson statistics, the counting LLR significance is defined as:

$$S_{cL} = \sqrt{2((N_s + N_b)\ln(1 + N_s/N_b) - N_s)}. \quad (2)$$

The observed width of the Higgs boson signal is the convolution of the natural width and of the experimental resolution. For low masses, the latter dominates while the natural width of the Higgs boson becomes significant at masses above $2 \times m_{\rm Z}$. In order to match the width of the expected signal distribution, the width of the sliding window is optimized as a function of the Higgs boson mass. Table 8 presents the values of the optimized width as a function of the Higgs boson mass. The significance is then evaluated for each central position of the (symmetrical) window, and the position which maximizes the significance is used for the determination of the expected number of background and signal events. Table 9 presents the number of signal and background events in this mass window, for each Higgs mass hypothesis.

$m_{\rm H}$ (GeV/c^2)	115-130	140-170	180-200	250	300
window size (GeV/c^2)	6	8	10	16	24

Table 8: Optimized window size as a function of the Higgs boson mass.

$m_{\rm H}$ (GeV/c^2)	115	120	130	140	150	160	170	180	190	200	250	300
N_s	1.52	2.97	8.18	15.80	17.19	8.38	3.76	9.95	34.05	38.20	27.68	21.69
N_b	2.26	1.94	3.71	4.31	3.68	3.10	3.37	6.42	14.62	17.29	13.40	7.63
$\delta N_b(exp.)$	0.063	0.089	0.126	0.167	0.105	0.148	0.145	0.187	0.551	0.505	0.466	0.187
$\delta N_b(th.)$	0.039	0.049	0.079	0.098	0.095	0.084	0.100	0.191	0.440	0.549	0.602	0.417

Table 9: Expected number of Higgs boson signal (N_s) and background (N_b) events in the optimized window, for an integrated luminosity of 30 fb^{-1}; systematic uncertainty on the background expectation, from experimental sources ($\delta N_b(exp.)$) and theoretical sources ($\delta N_b(th.)$); the systematic errors are given for an analysis where the ZZ$^{(*)}$ continuum is normalized to the measurement of single Z production.

Figure 15 shows the statistical significance S_{cP} as a function of the Higgs boson mass for a luminosity of 30 fb^{-1}. Similar results are obtained with the significance estimator S_{cL} and are also shown in Fig. 15. For $m_{\rm H}$ values below $2 \times m_{\rm Z}$, the significance follows the signal cross-section with a drop around $2 \times m_{\rm W}$ due to the opening of the WW$^{(*)}$ channel. For Higgs mass values greater than $2 \times m_{\rm Z}$, the significance evolves very slowly. The significance level expected for $m_{\rm H} \gtrsim 2 \times m_{\rm Z}$ is comparable to the one at 150 GeV/c^2 as the larger branching ratio H $\rightarrow$ ZZ is compensated by the increased ZZ$^{(*)}$ background. Also shown in Fig. 15 is the significance evaluated including the systematic uncertainties described in Section 6 for the "ZZ/Z" and "sidebands" methods.

Figure 16 shows the possible outcome of two MC experiments carried out for an integrated luminosity of 30 fb^{-1}. The examples given correspond to a "favorable" and a "less favorable" fluctuation.

Finally, Fig. 17 shows the integrated luminosity needed for a 5σ and 3σ discovery of the SM Higgs boson in the 4e decay channel as a function of the Higgs boson mass, with the systematic errors included using the ZZ/Z normalization method.

An extension of this analysis has been performed for Higgs boson masses above 300 GeV/c^2 and the H $\rightarrow 4$e results have been combined with H $\rightarrow 2$e2μ and H $\rightarrow 4\mu$ decay channels in Ref. [19]. The most significant feature in this very high mass region is the increase of the Higgs boson natural width, which translates into a necessary increase of the mass window size for event counting. Otherwise the production cross-section times branching ratio is subject to a slow evolution. A significance of 6.5 for the Higgs boson observation at $m_{\rm H} = 400$ GeV/c^2 is obtained for an integrated luminosity of 30 fb^{-1} with systematics extrapolated using the ZZ/Z method. The significance reduces to 2.5 for $m_{\rm H} = 600$ GeV/c^2.

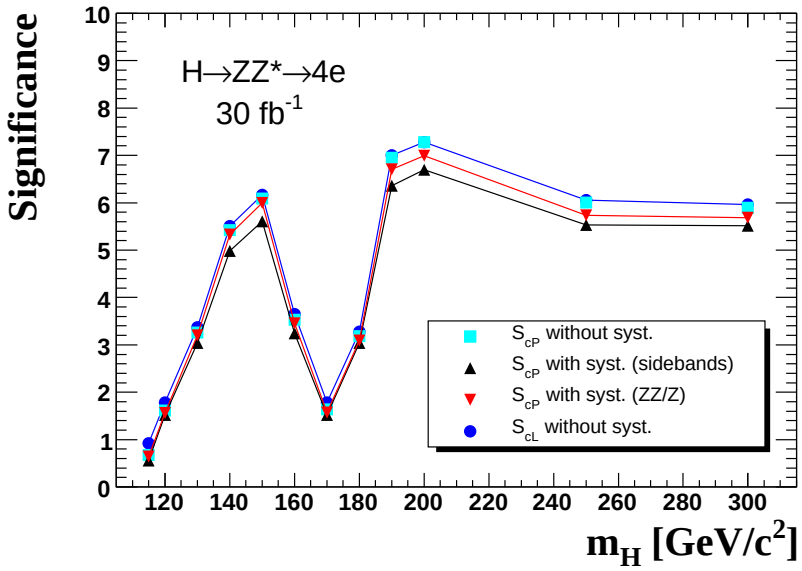

Figure 15: Significance of the SM Higgs boson observation via the H $\rightarrow$ $4e$ channel in the CMS experiment at the LHC. S_{cP} significance estimator as a function of $m_{\rm H}$ of the SM Higgs boson observation for an integrated luminosity of 30 fb^{-1}; the S_{cL} significance estimator is also shown for comparison. The significance S_{cP} is shown as obtained without and with systematic errors included, and for systematic errors obtained either by controling backgrounds using sidebands, or in an analysis where the ZZ$^{(*)}$ continuum is normalized to the single Z production.

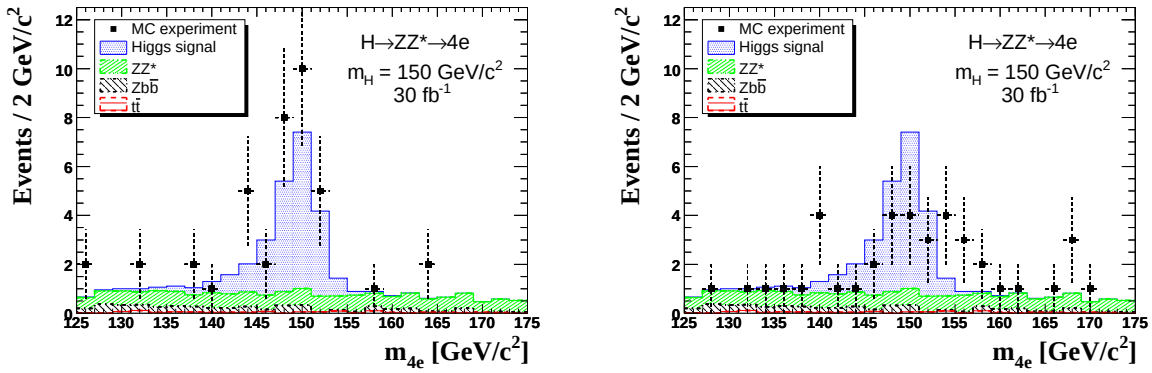

Figure 16: Example of single MC experiments corresponding to an integrated luminosity of 30 fb^{-1}; a) example of a "favorable" case; b) example of an "unfavorable" case. The Poisson probabilities to observe in a single experiment a Higgs boson signal more significant than in case a), or less significant than in case b), are about 5%.

7.2 Mass and Cross-Section Measurements

The precision on the estimation of the Higgs boson mass depends on the quality of the reconstructed electrons and can, in general, be improved using event-by-event errors on the electron momentum estimation [24].

A fit of the $m_{4\rm e}$ mass distribution can be used to extract simultaneously the mass and cross-section observables. The estimate of the total cross-section is obtained from the fitted number of signal events corrected for the overall acceptance. The width measurement is possible only for Higgs boson masses above $\gtrsim 2 \times m_{\rm Z}$ where the natural width becomes the dominant factor.

As an alternative to the fit procedure, the Higgs boson mass can be estimated by computing the mean of the measurements inside the signal window. It is expected that, in the early stage of a Higgs boson discovery, such a mass estimate will be more robust, and, for low statistics, the only possible method for the Higgs boson mass measurement.

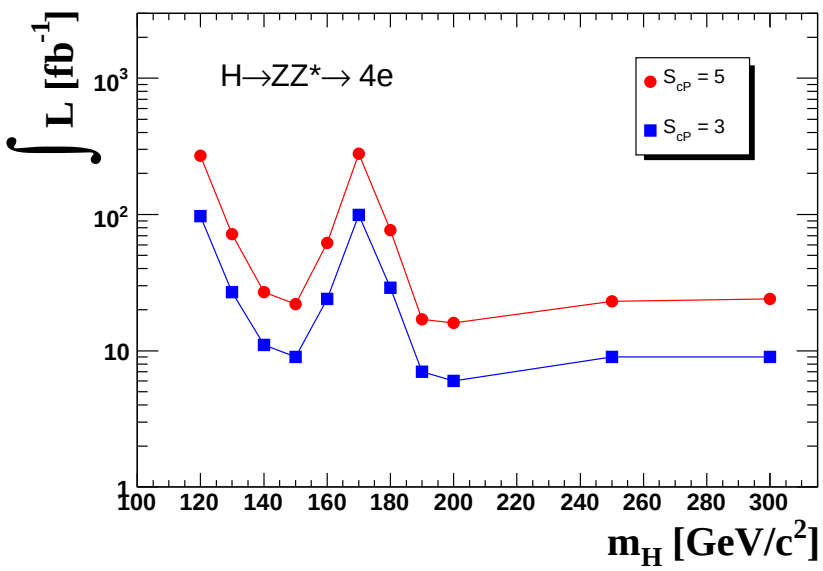

Figure 17: The integrated luminosity needed for a 5σ and a 3σ discovery via the $\mathrm{H} \rightarrow 4e$ channel including the systematic errors as obtained in the analysis method relying on a normalization of the $\mathrm{ZZ}^{(*)}$ to single Z production.

7.2.1 Mass Reconstruction and the 4e Event Topologies

The reconstruction provides for each electron an event-by-event error on the momentum estimation [24]. These momentum errors are propagated to an error on the $m_{4\mathrm{e}}$ estimation, neglecting the contribution from the error on electron tracks direction. In order to account for the non Gaussian part of the reconstructed electron momentum distributions, a small scaling is applied on the resulting $m_{4\mathrm{e}}$ error estimation, depending on the classifications of the four electrons. The computed 4 electron invariant mass error is presented for Higgs boson signal events in Fig. 18a for the different possible event topologies resulting from combinations of electrons of various classes. A projection for two specific event topologies is shown in Fig. 18b.

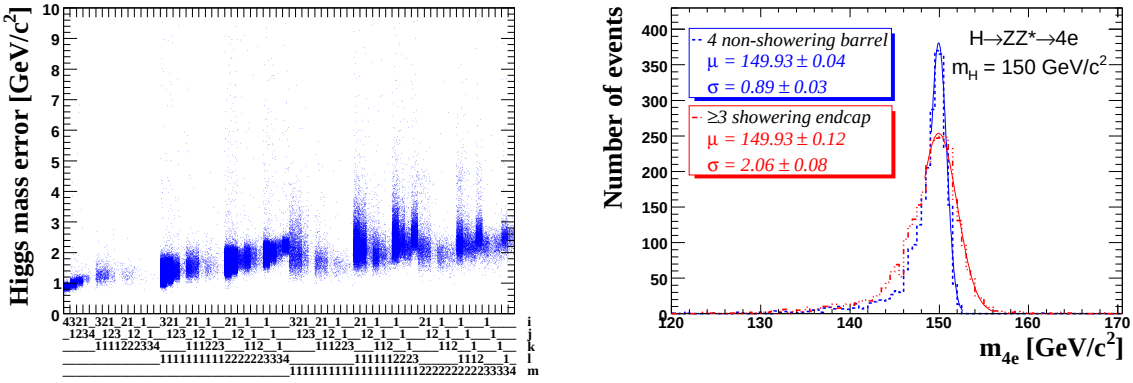

(a) (b)

Figure 18: Mass measurement errors for the signal for $m_{\mathrm{H}} = 150$ GeV$/c^2$. a) Error dependence on the electron classes; the integers on the abscissa give for each $4\mathrm{e}$ event topology the number of contributing electrons classified as *i = non-showering barrel*, *j = entering cracks*, *k = non-showering endcap*, *l = showering barrel*, and *m = showering endcap*. b) Example of $4\mathrm{e}$ reconstructed mass distribution for two different $4\mathrm{e}$ event topologies.

Event candidates built for instance from four *non-showering* electrons in the ECAL barrel (1.76% of the event candidates) clearly allow for a much better $m_{4\mathrm{e}}$ measurement (smallest errors on average and least dispersion of the mass measurement errors) than candidates built from three or more *showering* electrons in the ECAL endcaps. Over the full acceptance, about 36.7% of the event candidates contain three or more *showering* electrons.

7.2.2 Fit and Mean Methods

In the fit method, the signal contribution is modelled with two Gaussians, describing respectively the core and the low mass tail of the signal m_{4e} distribution. The relative fraction of events in the tail contribution as well as its mean and dispersion are determined by fitting the expectation for the "signal only" distribution, and are then fixed. The density of background events, in a sufficiently narrow mass range around the signal region, is taken as constant for any m_H hypothesis up to $m_H \approx 2 \times m_Z$, and modelled with a linear function for higher Higgs boson masses. A likelihood fit is performed to determine the background rate from sidebands and to extract the parameters of the the signal contribution. Three measured parameters are extracted for the signal: the mean and standard deviation of the core Gaussian contribution, and the total number of signal events.

In order to estimate the precision that could be reached in a typical experiment, the likelihood fit is performed on each of a large number of MC experiments, for each Higgs boson mass hypothesis and for several values of the integrated luminosity. The distributions of each of the three measured parameters are then fitted by Gaussians. For a given m_H and integrated luminosity, the mean expected Higgs boson mass reconstructed and the corresponding uncertainty are obtained from the distribution of the core "mean" values. The mean expected mass resolution and the associated uncertainty are obtained from the distribution of the core "standard deviation" values. The mean expected Higgs boson production cross-section measurement and associated uncertainty is derived from the distribution of the total number of signal events from each MC experiment.

As an alternative for the determination of the Higgs boson mass, a simple mean of the m_{4e} distribution for events inside the signal window can be computed. The accuracy and precision that could be reached in a typical experiment is obtained here again considering a large number of MC experiments.

The results for the mass measurements are presented in Fig. 19. This figure shows the relative difference between the measured mass, determined via either the fit or the mean method, and the generated Higgs boson mass, for an integrated LHC luminosity of 30 fb^{-1}. In the cases where the expected statistics is too low for the fit to be stable, only the results from the mean method are shown. The fit method provides an accurate estimation of m_H. A systematic bias on the mass estimate for low masses is observed for the estimate via the mean method and is caused by the asymmetric shape of the reconstructed signal. Over the considered mass range the fit gives a precision on the Higgs mass ranging from 0.5% to about 1%. The mean method provides a precision ranging from 0.2% to about 0.6%. The evolution of the mass measurement precision with the integrated luminosity for a 150 GeV/c^2 Higgs boson is also shown. The precision improves to about 0.35% for 60 fb^{-1}.

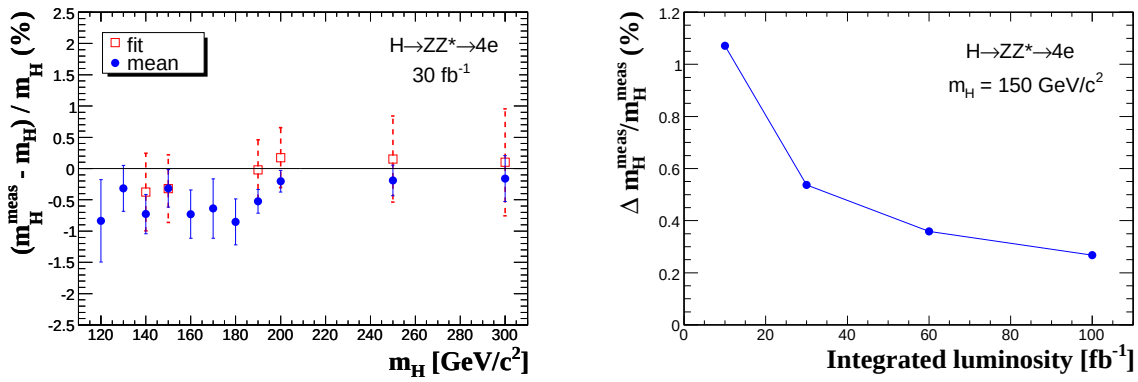

(a) (b)

Figure 19: a) Relative difference between the fitted mass (squares) or the weighted mean (dots) and the generated Higgs boson mass as a function of the generated Higgs boson mass and for a 30 fb^{-1} integrated luminosity. b) Precision of the Higgs boson mass measurement from the fit as a function of the integrated luminosity for a 150 GeV/c^2 generated Higgs boson mass.

The relative difference between the measured and the generated cross-section is shown in Fig. 20 for an integrated luminosity of 30 fb^{-1}. An accurate measurement of the cross-section is obtained over the full mass range considered here, with a bias below 5% for Higgs boson masses up to $\simeq$ 200 GeV and below 10% for $200 < m_H < 300$ GeV/c^2. The precision of the cross-section measurement is between 20 and 30%. In view of this statistical precision, the influence of detector systematics (about 5%) and of the uncertainty on the luminosity measurement (about 3% for 30 fb^{-1}) is expected to be marginal. The evolution of the cross-section measurement precision with the integrated luminosity and for a 150 GeV/c^2 Higgs boson is also shown. The precision improves

to about 15% for 60 fb^{-1}.

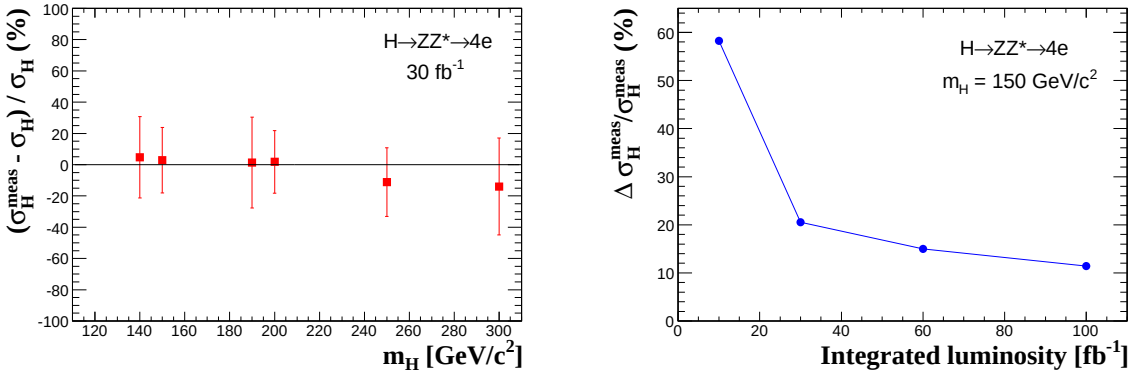

(a) (b)

Figure 20: a) Relative difference between the cross-section estimation and the true cross-section as a function of the Higgs boson mass for a 30 fb^{-1} integrated luminosity. b) Precision of the Higgs boson production cross-section measurement as a function of the integrated luminosity and for a 150 GeV/c^2 Higgs boson mass.

The natural width of the Higgs boson for $m_{\mathrm{H}} \lesssim 2 \times m_{\mathrm{Z}}$ is well below the detector resolution. Above this threshold, a measured width of 2.3 GeV/c^2 for $m_{\mathrm{H}} = 200$ GeV/c^2 and 4.2 GeV/c^2 for $m_{\mathrm{H}} = 300$ GeV/c^2 is obtained from the fit for an integrated luminosity of 60 fb^{-1}.

8 Conclusions

A prospective analysis has been performed for the search of a singly produced Standard Model Higgs boson decaying in a ZZ$^{(*)}$ pair. The presented analysis focuses on the $\mathrm{e^+e^-e^+e^-}$ final state making use of detailed electron reconstruction algorithms. A special attention is given to an efficient reconstruction of low p_T^{e} electrons and to the propagation of electron momentum errors dependent on observed track-supercluster patterns. The usage of electrons from Standard Model single Z production followed by $\mathrm{Z} \rightarrow \mathrm{e^+e^-}$ decay is shown to allow to control with precision the sources of systematic errors associated with the electron measurements. A novel technique relying on a Gaussian Sum Filter electron tracks is introduced to control the integral amount of tracker material in front of the CMS electromagnetic calorimeter, which affects the pattern of bremsstrahlung emission in the tracker volume. An optimized strategy based on a simple cut technique is presented for the search and discovery of the Standard Model Higgs boson in a low luminosity configuration of the LHC collider. Different means of controlling the amount of background are compared.

For an integrated LHC luminosity of 30 fb^{-1}, a Standard Model Higgs boson would be observed in the $\mathrm{e^+e^-e^+e^-}$ channel with a significance above 3 standard deviations for masses m_{H} in the range from about 130 to 160 GeV/c^2 and above 180 GeV/c^2. A significance of 5 standard deviations is reached around $m_{\mathrm{H}} \simeq 150$ GeV/c^2 and in the range from about 190 to 300 GeV/c^2. An accurate measurement of m_{H} is obtained from a fit to the measured mass distribution. A bias below 1%, and a precision ranging from 0.2% to about 0.6% is obtained from a simple mean over the events in the signal region. The production cross-section is measured with an accuracy better than 10% and a precision between 20 and 30%.

9 Acknowledgments

We wish to thank the conveners of the CMS PRS Ecal-e/γ Working Group for their support and suggestions. Thanks to our colleagues involved in the $\mathrm{H} \rightarrow 4\mu$ and $\mathrm{H} \rightarrow 2\mathrm{e}2\mu$ analyses and to the PRS Higgs Working Group convener for useful discussions. Thanks to general PRS conveners and CMS internal referees for their help during the finalization of this paper.

References

[1] R. Barate *et al.* [LEP Working Group for Higgs boson searches], Phys. Lett. B **565** (2003) 61-75.

[2] L. Babukhadia *et al.* [CDF and D0 Working Group Members], "Results of the Tevatron Higgs sensitivity study," FERMILAB-PUB-03-320-E.

[3] CMS Collaboration, "The Compact Muon Solenoid - Technical Proposal", CERN/LHCC 94-38.

[4] CMS Collaboration, "CMS Physics Technical Design Report Volume I", CERN/LHCC 2006-001.

[5] F. Beaudette *et al.*, "Search for a Light Standard Model Higgs Boson in the $\mathrm{H} \rightarrow \mathrm{WW}^{(*)} \rightarrow \mathrm{e}^{+}\nu\mathrm{e}^{-}\bar{\nu}$ Channel", CMS NOTE-2006/114.

[6] J. Pumplin, D. R. Stump, J. Huston, H. L. Lai, P. Nadolsky and W. K. Tung, JHEP **0207** (2002) 012.

[7] P. Golonka and Z. Was, Eur. Phys. J. C **45** (2006) 97-107;
E. Barberio and Z. Was, Comput. Phys. Commun. **79** (1994) 291-308;
E. Barberio, B. van Eijk and Z. Was, Comput. Phys. Commun. **66** (1991) 115-128.

[8] T. Sjostrand, L. Lonnblad and S. Mrenna, "PYTHIA 6.2: Physics and manual", arXiv:hep-ph/0108264.

[9] CMKIN, "CMS Interface for Event Generators", http://cmsdoc.cern.ch/cmsoo/projects/CMKIN.

[10] M. Spira, Nucl. Instrum. and Meth. A **389** (1997) 357-360;
M. Spira, "HIGLU: A Program for the Calculation of the Total Higgs Production Cross Section at Hadron Colliders via Gluon Fusion including QCD Corrections", arXiv:hep-ph/9510347.

[11] A. Djouadi, J. Kalinowski and M. Spira, Comput. Phys. Commun. **108** (1998) 56-74.

[12] S. Eidelman *et al.* [Particle Data Group], Phys. Lett. B **592** (2004) 1-1109.

[13] C. Zecher, T. Matsuura and J. J. van der Bij, Z. Phys. C **64** (1994) 219-226.

[14] CompHEP Collaboration, E. Boos *et al.*, Nucl. Instrum. Meth. A **534** (2004) 250-259;
A. Pukhov *et al.*, "CompHEP - a package for evaluation of Feynman diagrams and integration over multi-particle phase space", Moscow State U. preprint INP-MSU-98-41-542.

[15] S. Abdullin *et al*, "Search Strategy for the Standard Model Higgs Boson in the $\mathrm{H} \rightarrow \mathrm{ZZ}^{(*)} \rightarrow 4\mu$ Decay Channel using $M(4\mu)$-Dependent Cuts", CMS NOTE-2006/122.

[16] S. Abdullin *et al.*, "Relative contribution of t- an s- channels to the $\mathrm{H} \rightarrow \mathrm{ZZ}^{(*)} \rightarrow 4\mu$ process", CMS NOTE-2006/057.

[17] J. M. Campbell and R. K. Ellis, "MCFM - Monte Carlo for FeMtobarn processes", http://mcfm.fnal.gov.

[18] S. R. Slabospitsky and L. Sonnenschein, Comput. Phys. Commun. **148** (2002) 87-102.

[19] CMS Collaboration, "CMS Physics Technical Design Report Volume II", CERN/LHCC 2006-021.

[20] M. Beneke *et al.*, "Top quark physics", CERN preprint CERN-TH-2000-100.

[21] OSCAR, "Object-oriented Simulation fo CMS Analysis and Reconstruction", http://cmsdoc.cern.ch/OSCAR.

[22] S. Agostinelli *et al.*, Nucl. Instrum. Meth. A **506** (2003) 250-303.

[23] ORCA, "Object-oriented Reconstruction for CMS Analysis", http://cmsdoc.cern.ch/ORCA.

[24] S. Baffioni *et al.*, "Electron Reconstruction in CMS", CMS NOTE-2006/040.

[25] CMS Collaboration, "The Electromagnetic Calorimeter Project - Technical Design Report", CERN/LHCC 97-23.

[26] S. Cucciarelli, M. Konecki, D. Kotlinski and T. Todorov, "Track reconstruction, primary vertex finding and seed generation with the Pixel Detector", CMS NOTE-2006/026.

[27] CMS Collaboration, "The Tracker Project - Technical Design Report", CERN/LHCC 98-6, *idem*, "Addendum to the Tracker TDR", CERN/LHCC 2000-016.

[28] CMS Collaboration, "The Trigger and Data Acquisition Project", Volume I, CERN/LHCC 2000-038.

[29] E. Meschi, T. Monteiro, C. Seez and P. Vikas, "Electron Reconstruction in the CMS Electromagnetic Calorimeter", CMS NOTE-2001/034.

[30] L. Agostino and M. Pieri, "HLT Selection of Electrons and Photons", CMS NOTE-2006/078.

[31] CDF Collaboration, A. Abulencia *et al.*, "Measurements of inclusive W and Z cross sections in p anti-p collisions at s**(1/2) = 1.96-TeV", arXiv:hep-ex/0508029.

[32] S. Abdullin *et al.*, "Study of PDF and QCD scale uncertainties in the $pp \to \mathrm{H} \to \mathrm{ZZ}^{(*)} \to 4\mu$ events at the LHC", CMS NOTE-2006/068.

[33] P. Meridiani and R. Paramatti, "Use of $\mathrm{Z} \to \mathrm{e}^{+}\mathrm{e}^{-}$ events for ECAL calibration", CMS NOTE-2006/039.

[34] S. I. Bityukov and N. V. Krasnikov, Mod. Phys. Lett. A **13** (1998) 3235-3249.

[35] V. Bartsch and G. Quast, "Expected Signal Observability at Future Experiments", CMS NOTE-2005/004.